Flexoelectric Effect of Ferroelectric Materials and Its Applications

Dongxia Tian [1],* , **Dae-Yong Jeong [2],*** , **Zhenxiao Fu [3]** and **Baojin Chu [4,5]**

1. Institute of Advanced Materials, Hubei Normal University, Huangshi 435002, China
2. Department of Materials Science and Engineering, Inha University, 100 Inha-ro, Michuhol-gu, Incheon 22212, Republic of Korea
3. Guangdong Fenghua Advanced Technology Holding Co., Ltd., 18th Fenghua Road, Zhaoqing 526020, China
4. CAS Key Laboratory of Materials for Energy Conversion and Department of Materials Science and Engineering, University of Science and Technology of China, Hefei 230026, China
5. State Key Laboratory of Advanced Materials and Electronic Components, University of Science and Technology of China, Hefei 230026, China
* Correspondence: tdx_hzh@163.com (D.T.); dyjeong@inha.ac.kr (D.-Y.J.)

Abstract: The flexoelectric effect, which exists in all dielectrics, is an electromechanical effect that arises due to the coupling of strain gradients (or electric field gradients) with electric polarization (or mechanical stress). Numerous experimental studies have demonstrated that ferroelectric materials possess a larger flexoelectric coefficient than other dielectric materials; thus, the flexoelectric response becomes significant. In this review, we will first summarize the measurement methods and magnitudes of the flexoelectric coefficients of ferroelectric materials. Theoretical studies of the flexoelectric coefficients of ferroelectric materials will be addressed in this review. The scaling effect, where the flexoelectric effect dramatically increases when reducing the material dimension, will also be discussed. Because of their large electromechanical response and scaling effect, ferroelectric materials offer vast potential for the application of the flexoelectric effect in various physical phenomena, including sensors, actuators, and transducers. Finally, this review will briefly discuss some perspectives on the flexoelectric effect and address some pressing questions that need to be considered to further develop this phenomenon.

Keywords: flexoelectric; piezoelectric-like response; electromechanical coupling; ferroelectric materials

1. Introduction

Without an electric field, the strain and strain gradient contribute to the polarization in dielectric materials, which is expressed using the following equation [1]:

$$P_i = e_{ijk} S_{jk} + \mu_{ijkl} \frac{\partial S_{kl}}{\partial x_j} \tag{1}$$

where P_i is the electric polarization, S_{jk} is the strain, $\partial S_{kl}/\partial x_j$ is the strain gradient, e_{ijk} is the third-rank piezoelectric tensor, and μ_{ijkl} is the flexoelectric coefficient (the fourth-rank tensor). For the Einstein summation convention, i, j, k, and l traverse 1, 2, and 3, respectively. The first term describes the direct piezoelectric effect, where polarization is linearly related to a homogeneous strain in materials. The second term describes the direct flexoelectric effect, where polarization is linearly dependent on a strain gradient in dielectric materials. Thus, the flexoelectric effect is not restricted by material structures, thereby broadening electromechanical material options. There also exists a converse flexoelectric effect, as shown below [1]:

$$T_{ij} = \mu_{ijkl} \frac{\partial E_k}{\partial x_l} \tag{2}$$

where T_{ij} is the induced stress and $\partial E_k/\partial x_l$ is the electric field gradient.

The flexoelectric coefficient is a parameter that assesses the magnitude of the flexoelectric response. For low-symmetry materials, there are several non-zero components of the flexoelectric coefficient [2,3]. In centrosymmetric dielectric materials, the non-zero flexoelectric coefficient includes the longitudinal flexoelectric coefficient (μ_{1111}), transverse flexoelectric coefficient (μ_{1122}), and shear flexoelectric coefficient (μ_{1212}) [4]. The tensor matrices can be expressed as follows [4]:

$$\mu = \begin{pmatrix} \mu_{1111} & \mu_{1122} & \mu_{1122} & 0 & 0 & 0 \\ \mu_{1122} & \mu_{1111} & \mu_{1122} & 0 & 0 & 0 \\ \mu_{1122} & \mu_{1122} & \mu_{1111} & 0 & 0 & 0 \\ 0 & 0 & 0 & \mu_{1212} & 0 & 0 \\ 0 & 0 & 0 & 0 & \mu_{1212} & 0 \\ 0 & 0 & 0 & 0 & 0 & \mu_{1212} \end{pmatrix} \tag{3}$$

where μ_{1111}, μ_{1122}, and μ_{1212} can be written as μ_{11}, μ_{12}, and μ_{44} using Voigt tensor notations.

Flexoelectric coefficient scales for the dielectric susceptibility of materials were proposed [1,5] and are expressed as

$$\mu_{ijkl} = \gamma \chi_{ijkl} \frac{e}{a} \tag{4}$$

where χ_{ijkl} is the dielectric susceptibility, γ is the scaling factor, e is the electron charge, and a is the unit cell dimension. Using Equation (4), the flexoelectric coefficients of simple dielectrics were calculated to be as small as $10^{-11} \sim 10^{-10}$ C/m, which hindered the research interest in flexoelectricity [1,4–6]. In the early 2000s, Cross and coworkers measured a significant flexoelectric coefficient at the μC/m level in ferroelectric materials, which was much larger than the previously estimated values, attracting the attention of many researchers [1,4,6–12]. However, the theoretical explanations for this phenomenon remain elusive [4,6,11]. Several experimental results have demonstrated that extrinsic mechanisms dominate the measured flexoelectric coefficient of ferroelectric materials, which will be discussed in detail below.

The other important parameter, the strain gradient, depends on the elastic modulus, applied force, and material size. For example, the strain gradient in nanoscale materials is several orders of magnitude larger than that in bulk materials [4,6,13,14]. Thus, the flexoelectric response shows a strong scaling effect, which will also be discussed below [4,6,13,14]. Based on the large flexoelectric coefficients in ferroelectric materials and high strain gradients in small-scale dielectrics, several applications have been designed. Because the flexoelectric effect is also an electromechanical coupling effect, it can be applied in sensors, actuators, transducers, and energy harvesters [14–20]. Furthermore, some novel applications have been developed due to the universality of the flexoelectric effect, such as mechanical writing memory; manipulating oxygen vacancies and carriers; controlling ferromagnetic switching and band structures; and enhancing the thermoelectricity, photovoltage, and photocurrent [11,12,15,16].

In this review, we review the measurement methods and magnitudes of the flexoelectric coefficients, the theoretical investigations of the measured flexoelectric coefficients, the flexoelectric effect in nanoscale materials, and the applications of the flexoelectric effect, which are presented in Sections 2–6. Finally, the future directions of flexoelectricity are addressed in Section 7.

2. Measurement Methods of Flexoelectric Coefficients

The flexoelectric coefficient is the product of the linear coupling between polarization (or stress) and strain gradient (or electric field gradient). Therefore, to measure flexoelectric coefficients, methods of manipulating the strain gradient or electric field gradient of materials should be adopted. The methods for obtaining strain gradients include cantilever bending, four-point bending, three-point bending, point-ring bending, pyramid compression, and shock wave. In this section, we detail the methods for measuring flexoelectric coefficients. Table 1 includes nomenclatures used in Section 2.

Table 1. Nomenclatures used in Section 2.

Parameters	Meaning	Parameters	Meaning
F	Force	$w(x_1)$	Displacement of point x_1 for a cantilever beam
$\partial S_{kl}/\partial x_j$	Strain gradient	P	Polarization
i	Current	f	Measurement frequency
A	Electrode area	L	Distance from the free end to the clamping end of a cantilever beam
μ_{ijkl}	Flexoelectric coefficient	b	Width of a plate sample or edge length of the bottom square surface of a sample with a truncated pyramid-like shape
s	Speed of the top metal crosshead	t	Time
l	Distance of the outer span of a plate sample	Q	Charge
z_0	Displacement of the center point of a three-point bending sample	σ	Poisson ratio
h	Thickness of the sample	c_{11}	Elastic modulus
d_{33}	Piezoelectric coefficient	r	Distance of a point from the center of a disc sample
R_D	Radius of a disc sample	a	Edge length of the top square surface of a sample with a truncated pyramid-like shape
$u(x,t)$	Displacement of the particle at point x and time t using the shock-wave method	c	Shock-wave velocity
v	Speed of impacted sample by a flying plate	λ	Ratio of the flying plate to the sample mass
ρ	Mass density	U_{max}	Induced voltage from flexoelectric response
R	Resistance of a loading resistor	D_s	Diameter of a disc sample
γ	A deflecting micro-angle along the parallel lines of a cylinder-shaped sample	$d\varphi$	A rotating micro-angle along the diameter line of a cylinder-shaped sample
$\gamma_{r\varphi}$	Shear strain	M_n	Applied torque
J	Polar moment of inertia	G	Shear modulus

2.1. Cantilever Bending (CB)

One common method for obtaining strain gradients is the cantilever bending method (CB), which mainly measures μ_{12} [7–9]. The samples should be fabricated as rectangular shapes. As shown in Figure 1a, one end is kept clamped and the other free end is driven by force (F), which causes a bending deformation (i.e., strain gradient). The displacement $w(x_1)$ along the thickness direction (x_3) can be measured by a differential variable reluctance transducer for point x_1 (the distance from the clamping point) on the beam and is a function of x_1 [7]. At point x_1, the strain gradient $\partial S_{11}/\partial x_3$ can be calculated as follows [7]:

$$\frac{\partial S_{11}}{\partial x_3} = \frac{\partial^2 w(x_1)}{\partial x_1^2} \tag{5}$$

$w(x_1)$ can be calculated using the mode shape function [7]:

$$w_r(x_1) = A_r \left\{ \begin{array}{l} [\sin(\beta_r L) - \sinh(\beta_r L)][\sin(\beta_r x_1) - \sinh(\beta_r x_1)] \\ + [\cos(\beta_r L) - \cosh(\beta_r L)][\cos(\beta_r x_1) - \cosh(\beta_r x_1)] \end{array} \right\} \tag{6}$$

and

$$A_r = \frac{C_1}{\sin(\beta_r L) - \sinh(\beta_r L)} \tag{7}$$

where r is the fundamental mode and its value is usually 1; therefore, $\beta_1 L = 1.875$ [7]. L is the distance from the free end to the clamped end of the beam, and C_1 is determined by the measured vertical displacement of point x_1. The flexoelectric response generating a current (i) can be measured by a lock-in amplifier and is transformed into polarization (P):

$$P = \frac{i}{2\pi f A} \tag{8}$$

where f is the measurement frequency and A is the electrode area. After measuring the flexoelectric polarization and strain gradient of several points, μ_{12} can be calculated using the slope of the linear curve between the polarization and the strain gradient [9].
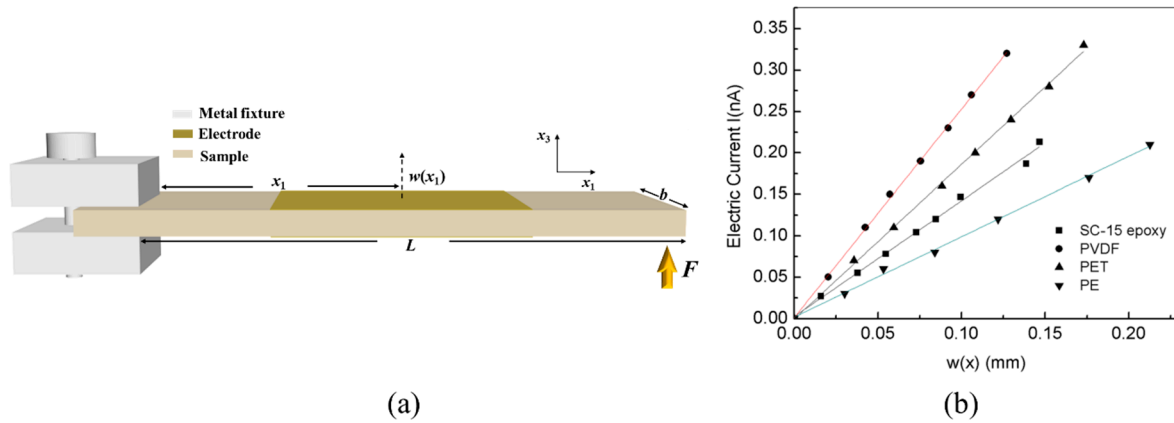
Figure 1. (**a**) Schematic of the cantilever bending method used to apply a strain gradient. The dotted arrow represents the displacement $w(x_1)$ of point x_1 when applying F to the free end of the beam. (**b**) The relationship between the electric current induced by the flexoelectric effect and the displacement of a specific point on the polymer beam. Reprinted with permission from [21]. Copyright 2012 AIP Publishing.

The above small electrodes are suitable for materials with significant flexoelectric coefficients. For materials with weak flexoelectric coefficients, the electrodes should be spread over both surfaces of the cantilever beam. In this case, μ_{12} can be derived using the linear ratio coefficient between i and $w(x_1)$ [21]:

$$i = \frac{2\pi f \mu_{12} bL}{x_1^2 (1 - (x_1/3L))} w(x_1) \tag{9}$$

where b is the width of the beam. As shown in Figure 1b, the flexoelectric coefficients can be obtained by fitting the linear relationship between i and $w(x_1)$ [21].

2.2. Four-Point Bending (4PB)

The four-point bending (4PB) method is also used to measure μ_{12} for a rectangular plate sample. As schematically shown in Figure 2a, both ends of the bottom side of a plate are supported by metal bars. Two forces from the metal bars on the top side compress the top side in the middle part of the sample through the metal crosshead, producing a large strain gradient $\partial S_{11}/\partial x_3$ along the thickness direction. The strain gradient can be calculated as follows [10]:

$$\frac{\partial S_{11}}{\partial x_3} = \frac{12st}{l^2} \tag{10}$$

where s is the speed of the top metal crosshead after applying F, t is the time, and l is the distance of the outer span. The generated polarization is

$$P = \frac{Q}{A} \tag{11}$$

where Q is the induced electric charge, which can be measured by an electrometer connecting the top and bottom electrodes, and A is the electrode area. Using Equations (10) and (11), μ_{12} is derived as

$$\mu_{12} = \frac{Ql^2}{12Ast} \tag{12}$$

As shown in Figure 2b, the flexoelectric coefficient measured using the 4PB method can be obtained according to the linear relationship between the polarization from the flexoelectric response and the strain gradient [10].

(a)   (b)
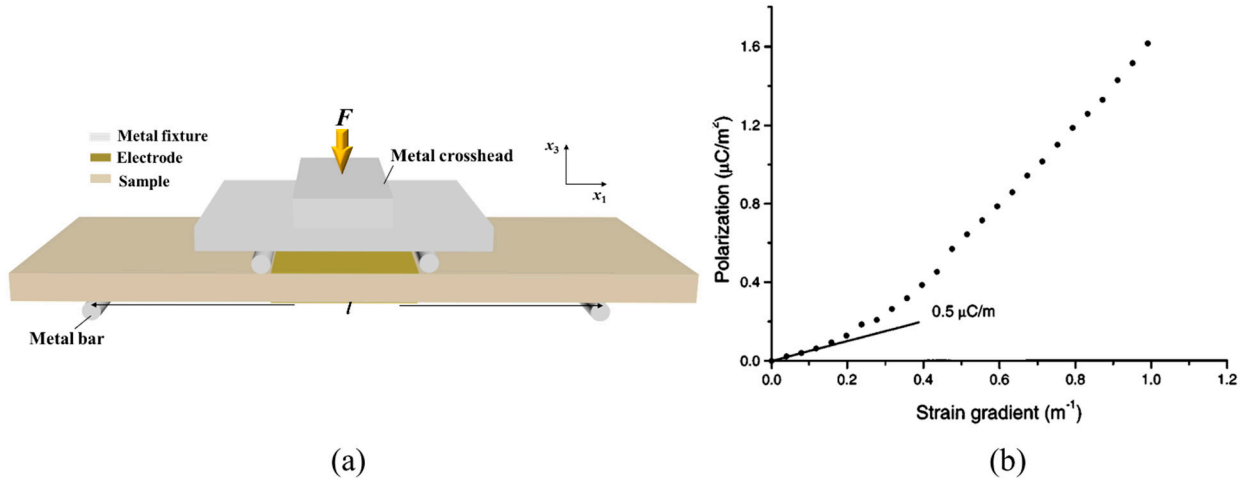
Figure 2. (**a**) Schematic of the four-point bending method used to apply a strain gradient. The four metal bars represent the four points. (**b**) Dependence of polarization on strain gradient for an unpoled PZT–5H sample induced during a 4PB test carried out at a crosshead speed of 0.2 mm/min. Reprinted with permission from [10]. Copyright 2003 AIP Publishing.

2.3. Three-Point Bending (3PB)

For the three-point bending method (3PB), both ends of the bottom side are also supported by metal bars but the middle part of the top side is compressed by one force, as shown in Figure 3a. The 3PB test fixture can be installed on a dynamic mechanical analyzer (DMA) or a d_{33} meter [22,23].

(a)   (b)
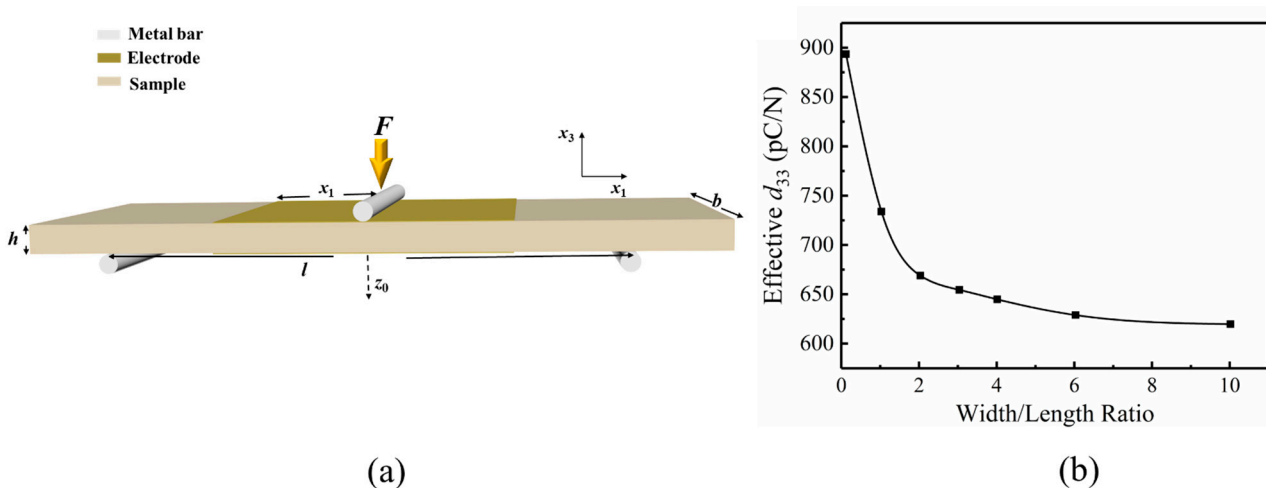
Figure 3. (**a**) Schematic of the three-point bending method used to apply a strain gradient. The three metal bars represent the three points. The dotted arrow represents the displacement of the center point when applying *F*. (**b**) The effect of the width-to-length ratio on the effective d_{33} from the flexoelectric response for rectangular $(Ba,Sr)TiO_3$ ceramics. Reprinted with permission from [23]. Copyright 2010 World Scientific.

Using a DMA, the generated current (*i*) from the flexoelectric response can be measured by a lock-in amplifier and is converted to polarization using Equation (8). The strain gradient in the thickness direction is denoted by [22]:

$$\frac{\partial S_{11}}{\partial x_3} = \frac{12z_0}{l^3}(l - x_1) \tag{13}$$

where z_0 is the displacement of the center point measured by the DMA, x_1 is the half length of the electrodes, and l is the distance of the outer span. From Equations (8) and (13), μ_{12} is derived as

$$\mu_{12} = \frac{il^3}{48\pi fbx_1z_0(l - x_1)} \tag{14}$$

The 3PB test can also be performed on a commercial d_{33} meter using a modified test fixture. For unpolarized materials, a d_{33} constant from the flexoelectric response can be measured. The relationship between μ_{12} and d_{33} can be given by [23]:

$$d_{33} = \frac{3\mu_{12}(1 - \sigma)l^2}{2h^3c_{11}} \tag{15}$$

where σ is the Poisson ratio of ceramics, h is the thickness, and c_{11} is the elastic modulus. Although the flexoelectric coefficient remains unchanged with the dimensions of ceramics in the micrometer size range, the magnitude of d_{33} was demonstrated to decrease with the increasing width-to-length ratio of a rectangular material (Figure 3b) because of the scaling effect of flexoelectricity [23].

2.4. Point-Ring Method (PR)

The point-ring method is used to measure the flexoelectric coefficients of disc ceramics. As shown in Figure 4, one side of a disc sample is supported by a metal ring with a comparable inner diameter and the middle of the other side is compressed by force (*F*), which causes bending deformation. The generated strain gradient in the thickness direction can be given by [24]:

$$\frac{\partial S(r)}{\partial x_3} = \frac{3F(1 - \sigma^2)}{\pi c_{11}h^3}\left(\frac{\sigma}{1 + \sigma} + \ln\frac{r}{R_D}\right) \tag{16}$$

where $S(r)$ is the strain along the radial direction, r is the distance of a point from the center of the disc, and R_D is the radius of the disc. The text fixture can also be mounted on a d_{33} meter. The measured d_{33} from the flexoelectric response is converted to the electric charge Q as follows:

$$d_{33} = \frac{Q}{F} \tag{17}$$

and the relationship between Q and the flexoelectric coefficient is

$$Q = 2\pi\int_{0+}^{R_D}\mu_\rho\frac{\partial S(r)}{\partial x_3}rdr \tag{18}$$

where μ_ρ is the effective flexoelectric coefficient that contains the contributions of μ_{12} and μ_{11}. Substituting Equations (16) and (17) into (18), μ_ρ can be expressed as:

$$\mu_\rho = \frac{2d_{33}c_{11}h^3}{3(1 - \sigma)^2R_D^2} \tag{19}$$

2.5. Pyramid Compression (PC)

The above methods for generating strain gradients are mainly realized by bending the samples. For samples with asymmetric shapes, such as truncated pyramid-like shapes, symmetric forces can induce strain gradients. Figure 5a shows that the forces from the top and bottom sides compress a sample with a truncated pyramid-like shape, which causes a strain gradient along the thickness direction. If the strain gradient $\partial S_{33}/\partial x_3$ is uniform, it can give [1]:

$$\frac{\partial S_{33}}{\partial x_3} = \frac{((F/c_{11}a^2) - (F/c_{11}b^2))}{h} = \frac{F(b^2 - a^2)}{c_{11}a^2b^2h} \tag{20}$$

where a and b are the edge lengths of the top and bottom square surfaces with electrodes, respectively. The proportionality coefficient between the generated polarization from the flexoelectric response and the strain gradient is μ_{11} (Figure 5b). However, the strain gradient cannot be simplified using Equation (20) and is nonuniformly distributed in pyramid-like samples [25]. Correspondingly, this method cannot obtain the exact value of μ_{11} [26]. Nevertheless, the simply calculated μ_{11} can be used to evaluate and compare the flexoelectric response of different materials. In addition, the method is not appropriate for materials with a piezoelectric response or polarized ferroelectric materials. Otherwise, the piezoelectric response would become an important factor in the measured flexoelectric response [26,27]. Thus, the contribution of the piezoelectric response should first be precluded when measuring the flexoelectric coefficient using the PC method [26]. For polymers, the strain can be caused by stretching the samples [28,29].
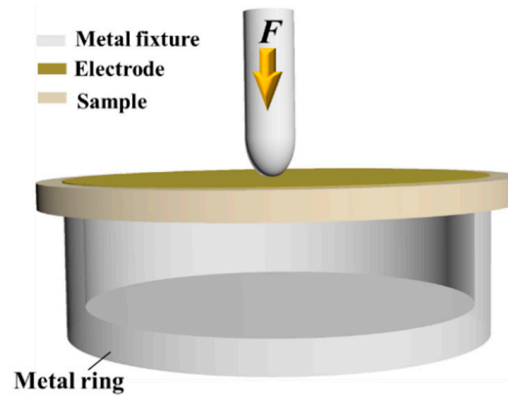

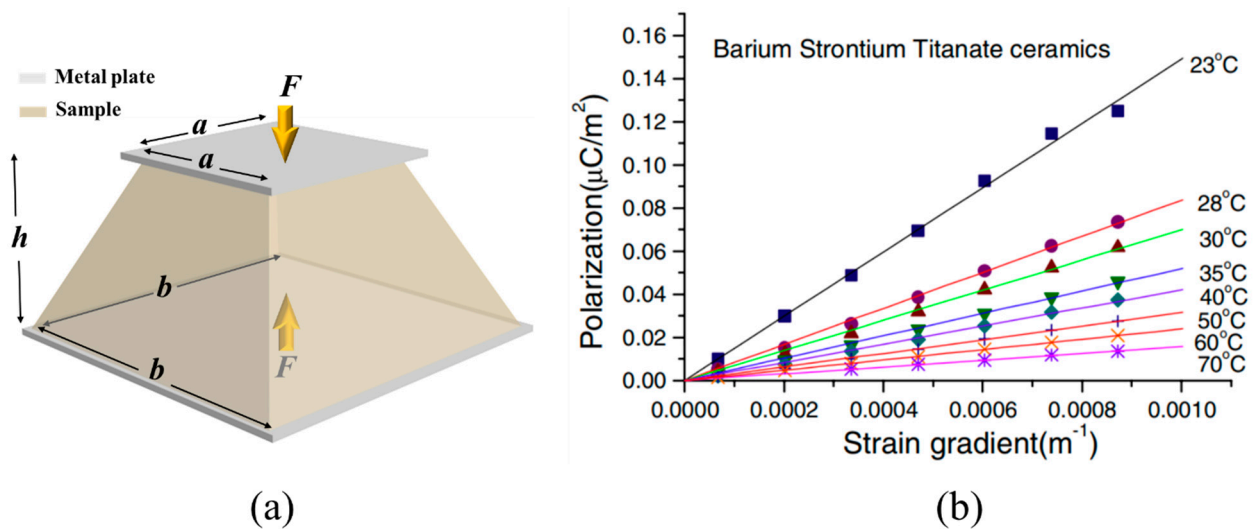**Figure 4.** Schematic of point-ring method used to apply strain gradient.

(a)

(b)

Figure 5. (**a**) Schematic of pyramid compression method used to apply strain gradient. (**b**) Dependence of polarization on strain gradient for an unpoled BST sample measured using the PC test at different temperatures. Reprinted with permission from [1]. Copyright 2006 Springer Science Business Media, Inc.

2.6. Shock-Wave Method

Shen and Liang used a shock wave propagating into a fixed sample to generate a strain gradient [30]. As shown in Figure 6, the first-order hydrogen gas gun shoots a flying slab, which causes a shock wave. The strain gradient is expressed as [30]

$$\frac{\partial^2 u(x,t)}{\partial x^2} = \frac{v}{c\lambda h_s}\left(e^{-\frac{ct-x-h_s}{\lambda h_s}} + e^{-\frac{ct+x-h_s}{\lambda h_s}}\right) \tag{21}$$

and

$$c = \sqrt{\frac{c_{11}(1-\sigma)}{\rho(1+\sigma)(1-2\sigma)}} \tag{22}$$

where $u(x,t)$ is the displacement of the particle at point x and time t, c is the wave velocity, v is the speed of the impacted sample by a flying plate, λ is the ratio of the flying plate to the sample mass, h is the thickness of the samples, ρ is the mass density of the materials, σ is the Poisson ratio of the samples, and c_{11} is the elastic modulus. The method measures μ_{11} by studying the relationship between the induced voltage $U_{\max}$ and strain gradient, which is given by

$$U_{\max} = \frac{R\mu_{11}v\pi D_s^2}{(2\lambda h)^2}\left(e^{-\frac{ct-x-h}{\lambda h}} + e^{-\frac{ct+x-h}{\lambda h}}\right) \tag{23}$$

where R is the resistance of the loading resistor and D_s is the diameter of the samples. Using this method, the measured μ_{11} of BaTiO$_3$ ceramics is ~17.33 µC/m, which is consistent with the published transverse flexoelectric coefficient.
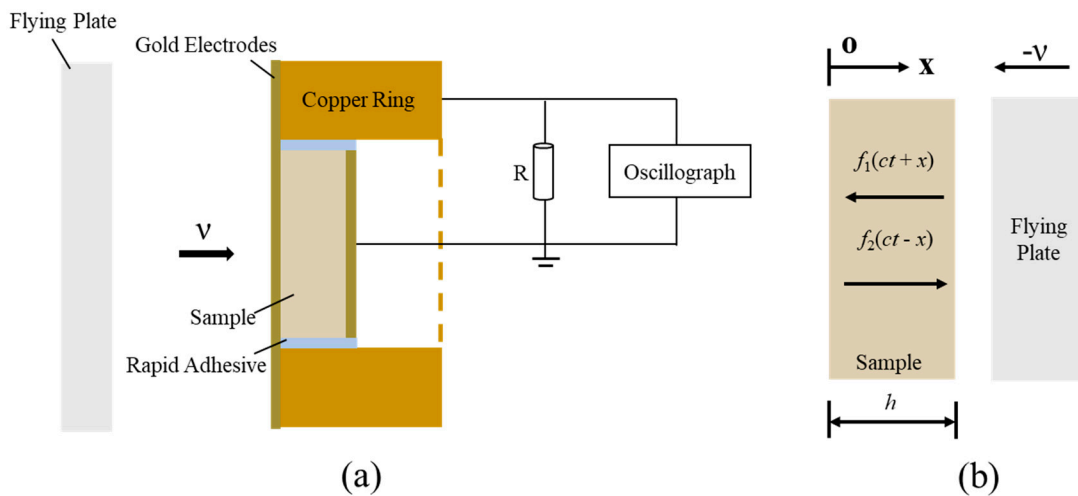
Figure 6. (**a**) Schematic of the sample configuration and the one-dimensional shock-wave experiment. (**b**) The theoretical model of the shock-wave experiment.

2.7. Cylinder Twisting (CT)

The cylinder twisting method is mainly designed for polymers and is used to measure the shear flexoelectric coefficients [31,32]. Both ends are clamped for a cylinder-shaped sample and the middle part is torqued, resulting in an inhomogeneous shear strain along the radial direction, as shown in Figure 7. Therefore, the strain gradient along the radial direction occurs when torque is exerted on the sample. Meanwhile, the parallel lines deflect at a micro-angle γ and the related diameter line rotates at a micro-angle $d\varphi$. The shear strain $\gamma_{r\varphi}$ in the effective region of the samples can be expressed as [31,32]

$$\gamma_{r\varphi} = \frac{M_n r}{JG} \tag{24}$$

where M_n is the applied torque, r is the radius, J is the polar moment of inertia of the effective region of the sample, and G is the shear modulus. The gradient of the shear strain along the radial direction can be given as [31,32]

$$\frac{\partial \gamma_r}{\partial r} = \frac{\gamma|_{r=R_D} - \gamma|_{r=r_D}}{R_D - r_D} = \frac{M_n}{JG} \tag{25}$$

Electric polarization is defined as

$$P_r = \mu_{44} \frac{\partial \gamma_r}{\partial r} \tag{26}$$

By substituting Equation (25) into Equation (26), the value of μ_{44} can be estimated. Before measuring the electric polarization, a tube-shaped sample is prepared and the intersurface and external surface of the tube are coated with full electrodes [31]. When applying torque to the sample, the electric polarization can be measured using a charge amplifier. The strain gradient is usually obtained through the torque angle φ [31,32]. The torque angle as a function of the applied torque M_n is [32]

$$\varphi = \int d\varphi = \int_0^l \frac{M_n}{JG} dz = \frac{M_n l}{JG} \tag{27}$$

where l is the total length of the specimen along the z direction. After measuring the torque angle and applied torque, the strain gradient can be estimated using Equations (25) and (27).
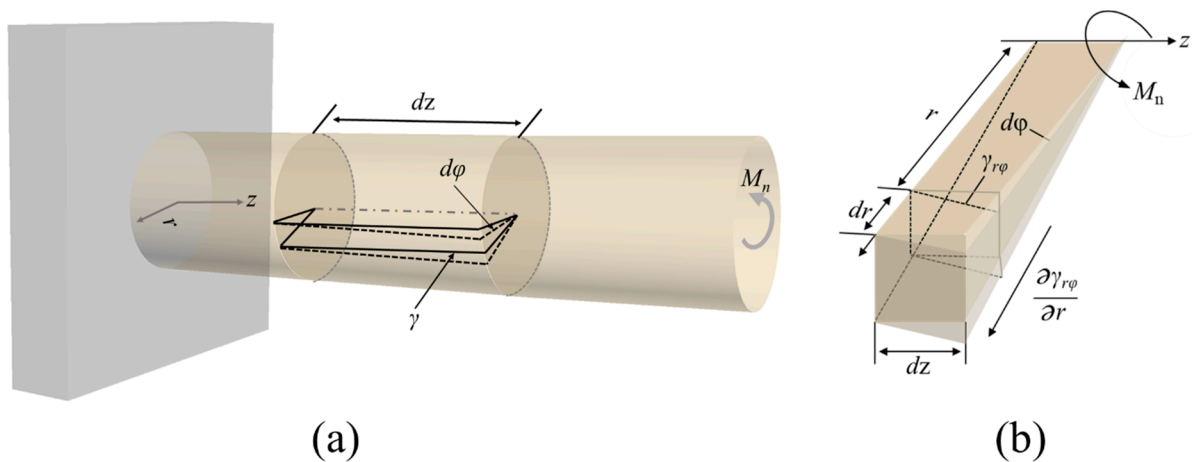
Figure 7. (**a**) Schematic of shear and deformation under the torque value. (**b**) Infinitesimal analysis of the shear strain gradient.

2.8. Converse Flexoelectric Effect (CFE)

For the converse flexoelectric response, the flexoelectric coefficients μ_{ijkl} can be calculated according to Equation (2). To apply an inhomogeneous electric field, measured materials with asymmetric shapes are usually required, such as those with truncated pyramid-like shapes [33,34]. An electric field gradient is generated when a voltage is applied on the top and bottom surfaces or both lateral sides of the truncated pyramid-like samples (Figure 8a,b) [33,34]. Figure 8c shows the relationship between the displacement of the trapezoid BST block from the converse flexoelectric effect and the applied voltages, which can be used to estimate the flexoelectric coefficient [33]. The flexoelectric coefficients obtained from the direct effect and converse effect should be the same for the same materials. The strain induced by the flexoelectric response can be monitored by a high-resolution laser vibrometer and converted to stress via the elastic modulus.
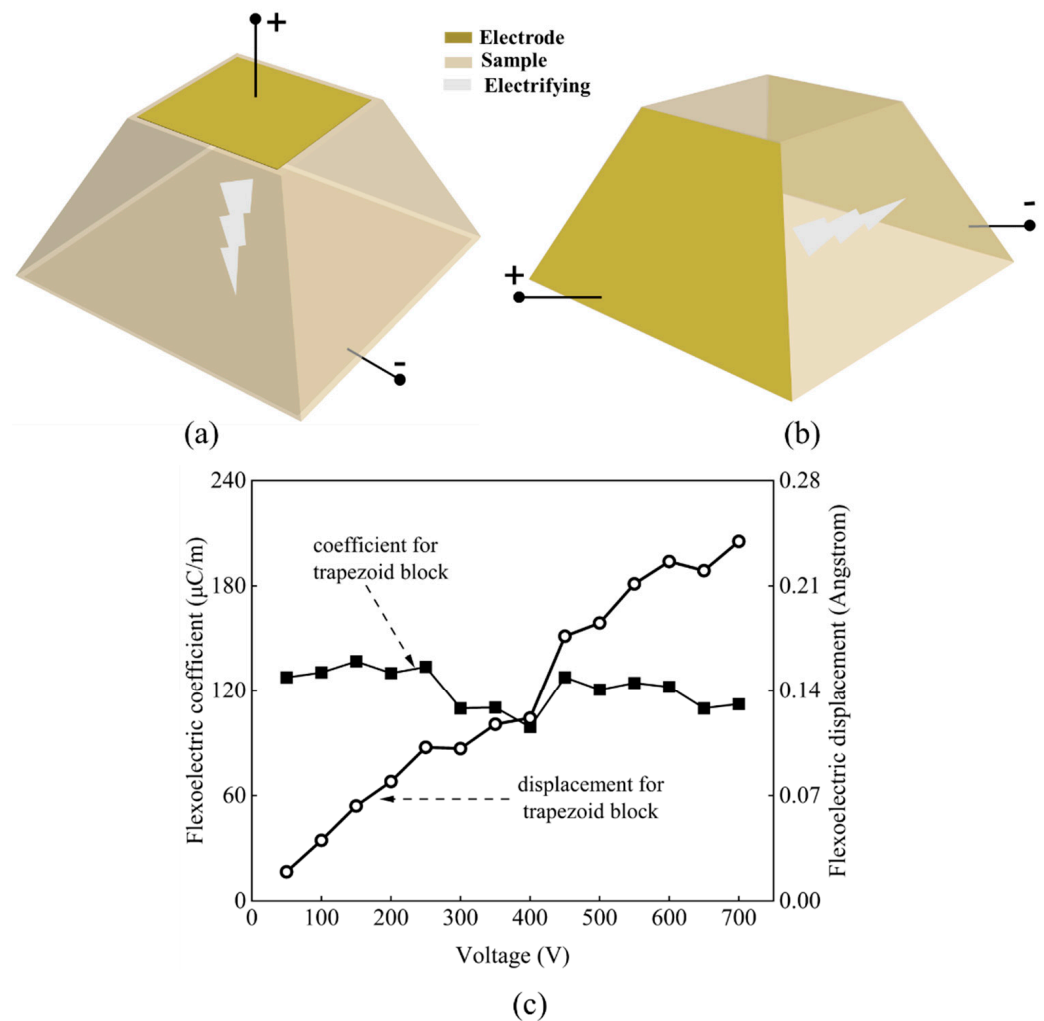
Figure 8. Schematic of converse flexoelectric coefficient measurement by applying a voltage on (**a**) top and bottom surfaces, or (**b**) both lateral sides of the truncated pyramid-like samples. (**c**) Flexoelectric coefficient and displacement of the trapezoid BST block measured by the converse flexoelectric effect at 25 °C under ac drive voltages with a frequency of 400 Hz. Reprinted with permission from [33]. Copyright 2006 AIP Publishing.

3. The Magnitude of the Flexoelectric Coefficient

The flexoelectric coefficients of different ferroelectric materials were measured using the methods described above and are summarized in Tables 2 and 3. It should be noted that a reliable comparison of the results presented in Tables 2 and 3 is impossible due to the lack of uncertainties in many of the results. The origin of the measured flexoelectric coefficient is complex and the flexoelectric coefficient in ferroelectric materials contains some inseparable non-zero components and extrinsic contributions (discussed in the next section). Thus, the measured flexoelectric coefficients are effective values [27]. For example, the measured μ_{11} comprises the contributions of μ_{11} and μ_{12}. In addition, the flexoelectric coefficients vary with the measurement methods for the same material, as shown in Tables 2 and 3, indicating that the comparison of flexoelectric coefficients should be based on the same measurement method.

Table 2. Summary of the measured flexoelectric coefficients of inorganic ferroelectric materials at room temperature.

Material	Flexoelectric Coefficient (Frequency)	Value, μC/m	Method
$Ba_{0.7}Sr_{0.3}TiO_3$ [35]	μ_{12} (17 Hz)	~7	CB
$Ba_{0.67}Sr_{0.33}TiO_3$ [1]	μ_{11} (0.5 Hz)	~150	PC
$Ba_{0.67}Sr_{0.33}TiO_3$ [33]	μ_{11} (400 Hz)	121 ± 20	CFE
$Ba_{0.67}Sr_{0.33}TiO_3$ [9]	μ_{12} (1 Hz)	~100	CB
$Ba_{0.67}Sr_{0.33}TiO_3$ [34]	μ_{12} (10 Hz)	124 ± 14	CFE
$Ba_{0.67}Sr_{0.33}TiO_3$ [36]	μ_{ρ} (110 Hz)	284 ± 20	PR
$Ba_{0.67}Sr_{0.33}TiO_3$ [37]	μ_{12}	6 ~10	3PB
$Ba_{0.65}Sr_{0.35}TiO_3$ [38]	μ_{12} (2 Hz)	~8	CB
$Ba_{0.6}Sr_{0.4}TiO_3$ [24]	μ_{ρ} (110 Hz)	10 ± 2	PR
$Ba_{0.6}Sr_{0.4}TiO_3/Ni_{0.8}Zn_{0.2}Fe_2O_4$ [39]	μ_{12} (30 Hz)	~128	CB
$Ba_{0.5}Sr_{0.5}TiO_3$ [36]	μ_{ρ} (110 Hz)	2 ± 0.5	PR
$SrTiO_3$ [36]	μ_{ρ} (110 Hz)	0.3 ± 0.02	PR
$SrTiO_3$ [40]	μ_{12} (9 Hz)	~0.008	CB
$SrTiO_3$ single crystals [22,41]	μ	0.001~0.01	3PB
20% C doped $SrTiO_3$ [40]	μ_{12} (9 Hz)	~0.16	CB
$Ba_{0.75}Sr_{0.25}TiO_3$ [42]	μ_{ρ} (110 Hz)	120 ± 20	PR
$BaTiO_3$ [43]	μ_{12}	~10	CB
$BaTiO_3$ [30]	μ_{11}	~17	Shock wave
$BaTiO_3$ single crystals [44]	μ_{13}^{eff} (13 Hz)	1~10	3PB
As prepared $BaTiO_3$ [45]	μ_{ρ} (110 Hz)	120 ± 20	PR
Abraded $BaTiO_3$ [45]	μ_{ρ} (110 Hz)	30 ± 5	PR
Quenched $BaTiO_3$ [45]	μ_{ρ} (110 Hz)	45 ± 5	PR
Heat-treated $BaTiO_3$ [45]	μ_{ρ} (110 Hz)	200 ± 20	PR
$BaTiO_3$-$0.08Bi(Zn_{0.5}Ti_{0.5})O_3$ [46]	μ_{12} (20 Hz)	~25	CB
$BaTi_{0.87}Sn_{0.13}O_3$ [47]	μ_{12} (30 Hz)	~53	CB
$BaTi_{0.85}Sn_{0.15}O_3$ [48]	μ_{12} (10 Hz)	~18	CB
0.5 wt%Al_2O_3-doped $BaTi_{0.85}Sn_{0.15}O_3$ [48]	μ_{12} (10 Hz)	~40	CB
0.2 wt%Al_2O_3-doped $BaTi_{0.85}Sn_{0.15}O_3$ [48]	μ_{12} (10 Hz)	~2	CB
$(Pb_{0.3}Sr_{0.7})TiO_3$ [1]	μ_{11} (0.5 Hz)	~21	PC
PMN [7]	μ_{12} (1 Hz)	~4	CB
0.9PMN-0.1PT [49]	μ_{11}	6~12	PC
0.9PMN-0.1PT [49]	μ_{11}	20~50	PC
0.9PMN-0.1PT [50]	μ_{33} (0.2 Hz)	~1000	CFE
PMN-PT single crystals [51]	μ_{13}^{eff} (13 Hz)	~10	3PB
PMN-PT single crystals [52]	μ_{eff} (3 Hz)	~71	CB
PMN-PT single crystals [52]	μ_{eff} (6 Hz)	~81	CB
PMN-PT single crystals [52]	μ_{eff} (9 Hz)	~99	CB
PMN-PT single crystals [52]	μ_{eff} (12 Hz)	~101	CB
PIN-PMN-PT single crystals [53]	μ_{eff} (9 Hz)	~50	CB
2.5% Bi-doped 0.7PMN-0.3PT [54]	μ_{12} (7 Hz)	~260	CB
2.5% Bi-doped 0.68PMN-0.32PT [54]	μ_{12} (7 Hz)	~300	CB
2.5% Bi-doped 0.66PMN-0.34PT [54]	μ_{12} (7 Hz)	~220	CB
2.5% Bi-doped 0.64PMN-0.36PT [54]	μ_{12} (7 Hz)	~80	CB
2.5% Sm-doped 0.70PMN-0.30PT [55]	μ_{12}	~430	CB
2.5% Sm-doped 0.68PMN-0.32PT [55]	μ_{12}	~550	CB
2.5% Sm-doped 0.66PMN-0.34PT [55]	μ_{12}	~490	CB
2.5% Eu-doped 0.66PMN-0.32PT [55]	μ_{12}	~380	CB
$Pb(Zr,Ti)O_3$ [10]	μ_{12}	0.5~2	4PB
$Pb(Zr,Ti)O_3$ [56]	μ_{12} (1 Hz)	~1.4	CB
Abraded PZT-81 [45]	μ_{ρ} (110 Hz)	5 ± 0.5	PR
Heat-treated PZT-81 [45]	μ_{ρ} (110 Hz)	25 ± 2.5	PR
Poled soft PZT [57]	μ_{12} (0.5 Hz)	~49	4PB
$PbZrO_3$ [58]	μ_{13}^{eff} (13 Hz)	~0.002	3PB
$AgNbO_3$ [58]	μ (13 Hz)	~0.005	3PB
NBT [59]	μ_{ρ} (110 Hz)	0.43 ± 0.02	PR

Table 2. *Cont.*

Material	Flexoelectric Coefficient (Frequency)	Value, μC/m	Method
NBBT2 [59]	μ_ρ (110 Hz)	0.83 ± 0.14	PR
NBBT6 [24,59]	μ_ρ (110 Hz)	6.1 ± 1.22	PR
NBBT8 [59]	μ_ρ (110 Hz)	4.19 ± 0.49	PR
Heat-treated NBBT8 [42]	μ_ρ (110 Hz)	20 ± 5	PR
Reduced NBBT8 [60]	μ_ρ (110 Hz)	1350 ± 100	PR
NBBT10 [59]	μ_ρ (110 Hz)	4.24 ± 0.95	PR
NBBT15 [59]	μ_ρ (110 Hz)	3.29 ± 0.2	PR
NBBT20 [59]	μ_ρ (110Hz)	3.25 ± 0.38	PR
NBBT20 [61]	μ_{12}	2.4 ± 0.5	CB
Reduced NBBT20 [61]	μ_{12}	100 ± 10	CB
$0.75BiFeO_3$-$0.25BaTiO_3$ [62]	μ_ρ (110 Hz)	1 ± 0.5	PR
Reduced $0.75BiFeO_3$-$0.25BaTiO_3$ [62]	μ_ρ (110 Hz)	140 ± 20	PR
$(Bi_{1.5}Zn_{0.5})(Zn_{0.5}Nb_{1.5})O_7/Ag$ [63]	μ_{12} (10 Hz)	~0.17	CB
$(K_{0.4}Na_{0.58}Li_{0.02})(Nb_{0.96}Sb_{0.04})O_3$ [64]	μ_{12}	~1	CB
$KTaO_3$ single crystals [41]	μ_{eff}	~0.004	3PB
$YAlO_3$ single crystals [41]	μ_{eff}	~−0.004	3PB
$DyScO_3$ single crystals [41]	μ_{eff}	~−0.008	3PB
$LaAlO_3$ single crystals [41]	μ_{eff}	~−0.003	3PB

Compound $Pb(Mg_{1/3}Nb_{2/3})O_3$ is abbreviated as PMN; $PbTiO_3$ is abbreviated as PT, and $Pb(Zr,Ti)O_3$ is abbreviated as PZT. Compound $1-x(Na_{1/2}Bi_{1/2})TiO_3$-$xBaTiO_3$ is abbreviated as NBBT(100x).

Table 3. Summary of the measured flexoelectric coefficients of ferroelectric polymers at room temperature.

Material	Flexoelectric Coefficient (Frequency)	Value, μC/m	Method
PVDF [21]	μ_{12} (21 Hz)	0.013 ± 0.001	CB
Oriented PET [21]	μ_{12} (21 Hz)	0.0099 ± 0.0004	CB
P(VDF-TrFE) [65]	μ_{12}	≤0.191 ± 0.017	CB
P(VDF-TrFE-CFE) [65]	μ_{12}	0.03 ± 0.0015	CB
PVDF [31]	μ_{12}	~0.00073	CT
α-phase bulk PVDF [26]	μ_{11}	~0.016	PC
PVDF [66]	μ_{12}	~0.015	CB
PVDF [66]	μ_{12}	~0.01	3PB
PVDF [66]	μ_{12}	~0.014	4PB
PVDF [67]	μ_{12} (6 Hz)	0.00582 ± 0.00043	CB
P(VDF-CTFE) [67]	μ_{12} (6 Hz)	0.00216 ± 0.00027	CB
P(VDF-HFP) [67]	μ_{12} (6 Hz)	0.00257 ± 0.00026	CB
PVDF/10 vol% BST [68]	μ_{12} (6 Hz)	0.00436 ± 0.00093	3PB
PVDF/15 vol% BST [68]	μ_{12} (6 Hz)	0.00681 ± 0.0007	3PB
PVDF/20 vol% BST [68]	μ_{12} (6 Hz)	0.00877 ± 0.00119	3PB
PVDF/25 vol% BST [68]	μ_{12} (6 Hz)	0.0135 ± 0.00176	3PB
P(VDF-TrFE) (70/30) [69]	μ_{12} (6 Hz)	0.00304 ± 0.00055	3PB
P(VDF-TrFE) (55/45) [69]	μ_{12} (6 Hz)	0.00418 ± 0.00067	3PB
P(VDF-TrFE-CTFE) [69]	μ_{12} (6 Hz)	0.00352 ± 0.0005	3PB

To enhance the flexoelectric coefficient, various attempts, including composite, doping, compositional gradient, or thermal treatment, can be adopted [39,45,48,54,61,70]. The flexoelectric coefficient of $Ba_{0.6}Sr_{0.4}TiO_3/Ni_{0.8}Zn_{0.2}Fe_2O_4$ composites was increased to ~128 μC/m compared to ~100 μC/m of $Ba_{0.6}Sr_{0.4}TiO_3$ ceramics [39]. In polymer materials, by adding 25% $Ba_{0.67}Si_{0.33}TiO_3$ to PVDF film, the flexoelectric coefficient was enhanced several times [68]. After doping Sm into $BaTi_{0.85}Sn_{0.15}O_3$ ceramics, the flexoelectric coefficient at room temperature can be greatly increased [55]. It was found that compositional gradients can greatly enhance the flexoelectric coefficient of ferroelectric ceramics [61]. The effective flexoelectric coefficient of reduced $0.92Na_{0.5}Bi_{0.5}TiO_3$-$0.08BaTiO_3$ (NBBT8) ceramics can be increased by more than two orders of magnitude after an asymmetric reduction

reaction using graphite, which causes a chemical inhomogeneity in the ceramics [60]. The high flexoelectric coefficients of the reduced ceramics can be maintained at a high temperature, as shown in Figure 9a [60]. When abraded ferroelectric ceramics are heat-treated at a temperature above the Curie temperature (T_C) or maximum dielectric temperature (T_m) and then slowly cooled, polarized surface layers are generated (discussed in detail in the next section), which contribute to the effective flexoelectric coefficient [45,59]. From the temperature dependence of the effective flexoelectric coefficient of BaTiO$_3$ ferroelectric ceramics (Figure 9b), it can be seen that μ_ρ of the slowly cooled sample sustains a high level, even at a temperature slightly higher than the Curie temperature [45]. Overall, the inorganic ferroelectric materials have a stronger flexoelectric response than ferroelectric polymers, as shown in Tables 2 and 3.
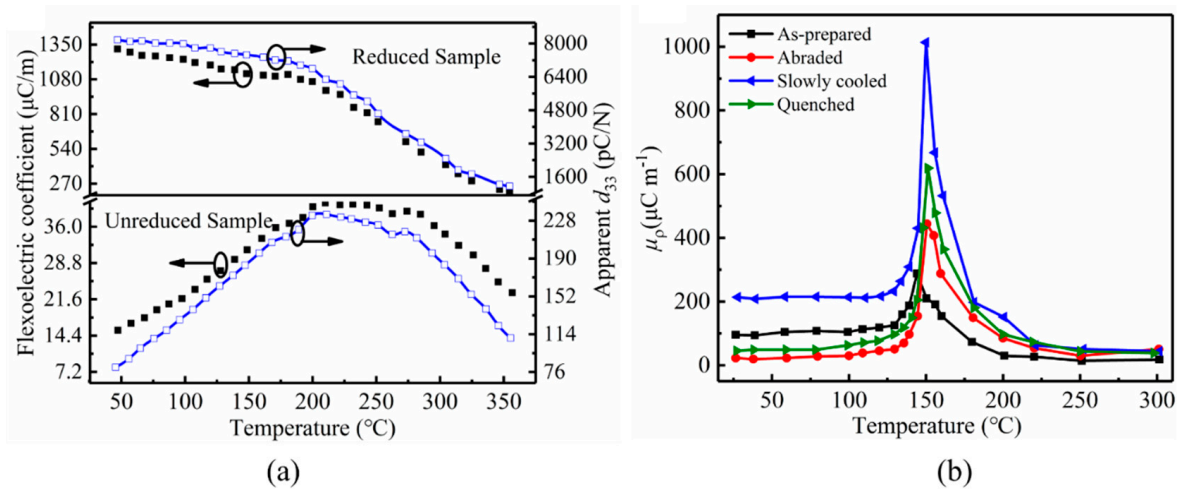
Figure 9. (**a**) The temperature dependence of the flexoelectric coefficient and apparent d_{33} for reduced and unreduced NBBT8 ceramics under bending. Reprinted with permission from [60]. Copyright 2018 Elsevier. (**b**) The temperature dependence of the flexoelectric coefficient for BaTiO$_3$ ceramics under bending. Reprinted with permission from [45]. Copyright 2018 American Physical Society.

4. Theoretical Studies of Measured Flexoelectric Coefficients of Ferroelectric Materials

In dielectric materials, the measured flexoelectric effect theoretically consists of contributions from bulk dynamic flexoelectricity, bulk static flexoelectricity, surface flexoelectricity, and surface piezoelectricity [1]. The bulk and surface flexoelectricity are theoretically proportional to the dielectric permittivity. In materials, each surface layer with a thickness of several atoms is always asymmetric, generating surface piezoelectricity [71–75]. Thus, the surface piezoelectricity is dependent on the surface properties [1]. Under bending, the surface piezoelectricity contributing to the flexoelectric response is manifested because one surface is in tension and the other is in compression. The magnitude of the flexoelectric effect is often evaluated using the flexocoupling coefficient f_{sjkl} and is given by [6]:

$$f_{sjkl} = \frac{\mu_{ijkl}}{\chi_{is}\varepsilon_0} \tag{28}$$

where ε_0 is the vacuum permittivity. Theoretically, f_{sjkl} is determined by the lattice parameter and should typically be below 10 V for common dielectric materials and ~15 V for materials with perovskite structures [6]. However, the experimental f_{sjkl} is often several orders of magnitude larger than the theoretically estimated values in ferroelectric materials, which implies that extrinsic mechanisms dominate the flexoelectric response in ferroelectric materials [36,42,45,59,60,62]. In this section, some theoretical investigations of the large flexoelectric coefficients of ferroelectric materials are summarized.

4.1. Theoretical Investigation of Spontaneously Polarized Surfaces

In ferroelectric ceramics, it has been demonstrated that spontaneously polarized surfaces with thicknesses of approximately several μm can be generated in ferroelectric materials, which is different from theoretical piezoelectric surfaces with thicknesses of several atoms [4,6,45,59]. The conditions for generating spontaneously polarized surfaces are that the ferroelectric ceramics should be slowly cooled from a temperature above T_C or T_m. During the heat-treatment process, a phase transition between the ferroelectric and paraelectric phases occurs, causing residual stress. Ceramics cooled at a high temperature are often accompanied by the release of stress. The extent of the stress release depends on the temperature. Since the grains on the surfaces are biaxially confined by the surrounding grains, the stress near the surfaces is mainly released along the thickness direction. Cooled from a temperature just above T_C or T_m, the stress in each surface with a thickness of ~10 μm releases inhomogeneously, causing a strain gradient and polarizing the surfaces. Under bending, one surface is tensile and another surface is compressive, generating a piezoelectric response that contributes to the measured flexoelectric-like response of ferroelectric ceramics (Figure 10a).
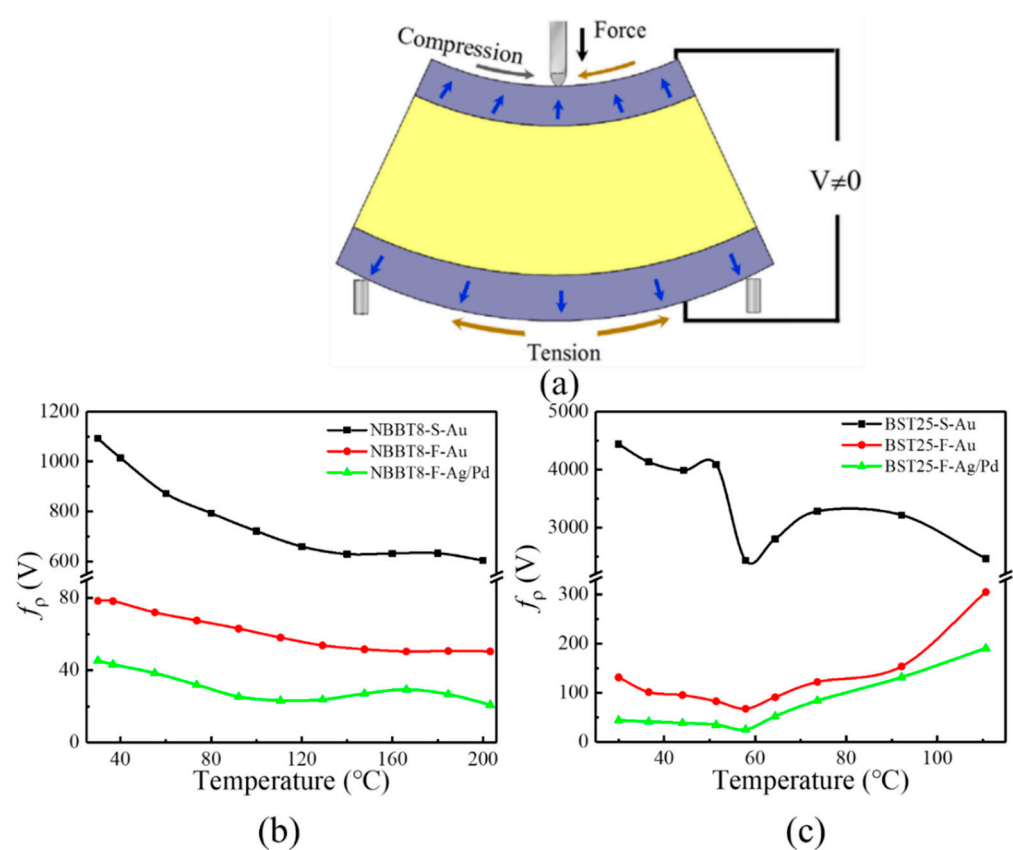
Figure 10. (**a**) Schematic of the contribution of the spontaneously polarized surface to the measured flexoelectric coefficient under bending. Reprinted with permission from [45]. Copyright 2018 American Physical Society. (**b**,**c**) The flexocoupling coefficients of NBBT8 and BST25 ceramics after sputtering (S) or fired (F)-on electrodes. Reprinted with permission from [42]. Copyright 2021 AIP Publishing. f_ρ is the effective flexoelectric coefficient.

To verify the extent of the surface effect contributing to the measured flexoelectric response, a fired-on metal electrode was used on the surfaces of ferroelectric ceramics. At a high firing temperature, the polarized surfaces can be destroyed [42]. At a high temperature that is lower than the firing temperature, the diffusion of substances in the electrode paste into the surface regions, stress relief, and the generation of impurity phases caused by volatile element evaporation occur, leading to a huge decay of the flexoelectric-like

response (Figure 10b,c) [42]. After suppressing the polarized surfaces, the flexocoupling coefficient can approach the intrinsic coefficient for $Ba_{0.75}Sr_{0.25}TiO_3$ (BST25) ceramics and $0.92Na_{0.5}Bi_{0.5}TiO_3$-$0.08BaTiO_3$ (NBBT8) ceramics, which confirms that the piezoelectric response from the polarized surfaces is the dominant mechanism that causes the large deviation of the measured flexoelectric-like response from the intrinsic response in ferroelectric ceramics. However, for $(Ba, Sr)TiO_3$ ceramics with a Sr content of less than 25 mol%, the polarized surfaces are challenging to remove using the fired-on electrode method. In addition, the flexocoupling coefficients of BST25 ceramics become much larger than the intrinsic coefficients at a temperature well above T_C, which may be ascribed to the polarized surfaces not being entirely removed by the fired-on electrode method or other extrinsic contributions to the flexoelectric-like response at a high temperature. Therefore, a new way to eliminate the polarized surfaces should be explored to quantify the contribution degree of the polarized surfaces to the measured flexoelectric response of ferroelectric ceramics.

The polarized surfaces also allow ferroelectric ceramics with sub-millimeter thicknesses to exhibit a non-negligible scaling effect, which reduces the weak-field dielectric properties, increases the coercive fields, and decreases the piezoelectric response [76].

4.2. Theoretical Investigation of Nanopolar Region Orientation Regulated by Strain Gradient

For relaxor ferroelectrics, it was thought that preexisting nanodomains or nanopolar regions have a significant effect on the measured flexoelectric response [8,51]. When external stress is applied to relaxor ferroelectrics, it easily induces a preferred orientation of the nanodomains or the nanopolar regions. In PMN relaxor ferroelectric ceramics, the nanodomains or nanopolar regions should possess eight equivalent <111> polarization orientations, which lack a preferred orientation. After bending deformation, the generated strain gradient breaks the balance of the polarization orientations, resulting in a preferable polarization orientation, which contributes to the large flexoelectric response of relaxor ferroelectric ceramics (Figure 11). It should be noted that this theory is aimed only at relaxor ferroelectrics, and the nanodomain contribution to the flexoelectric response has yet to be quantified.
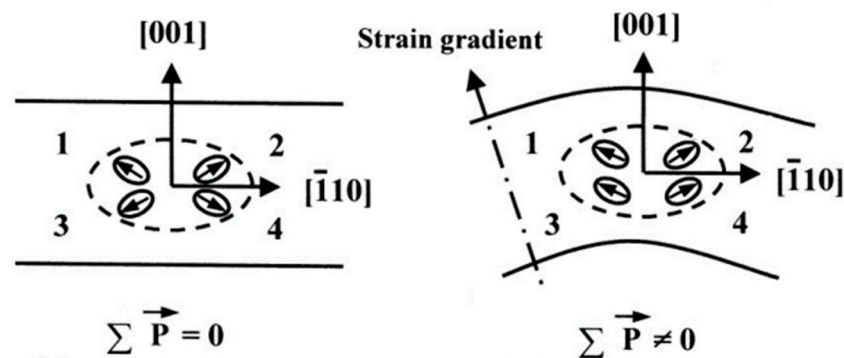

Figure 11. The orientation of nanodomains in relaxor ferroelectrics before and after applying a strain gradient. Reprinted with permission from [8]. Copyright 2001 AIP Publishing.

4.3. Theoretical Investigation of Inhomogeneity Inducing Symmetry Breaking

It was found that macroscopic symmetry breaking is inevitably generated in materials due to the inhomogeneity produced during preparation processes, resulting in built-in polarization [27]. During the densification of ceramics, the charged defects and polar nano-entities redistribute according to the initial position and direction of the samples and sintering temperature, determining the orientation of the built-in polarization (Figure 12). After applying the bending deformation, the measured flexoelectric response is enhanced by the piezoelectric response from the built-in polarization, which is thought to be the mechanism responsible for the large flexoelectric coefficients in ferroelectric materials. However, if the fabrication process is the main factor affecting the large flexoelectric response, the flexoelectric coefficients of identical ceramics prepared by different researchers

should be different due to inconsistent processing conditions. However, the reported flexoelectric coefficients of identical ceramics measured using the same methods are quite similar [22,36,40–42,59,60]. Therefore, macroscopic symmetry breaking may not be the primary cause of the measured large flexoelectric coefficients in ferroelectric materials.
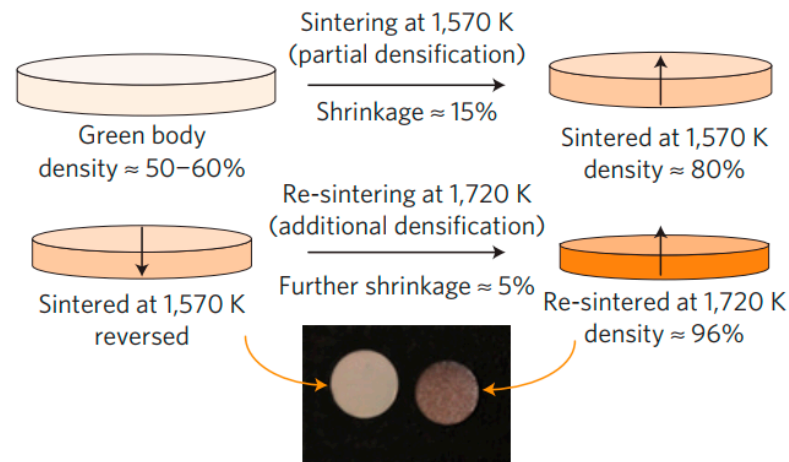
Figure 12. Breaking the macroscopic centric symmetry during sintering at high temperatures. The preferred direction of the polarization depends on the orientation of the sample in the furnace. The sample's arrow represents the polarization's preferred direction. Reprinted with permission from [27]. Copyright 2015 Springer Nature.

4.4. Theoretical Investigation of Barrier Layer

In addition to ferroelectrics, a significant flexoelectric coefficient can also be measured in semiconductors [77]. However, the above theories to explain the significant measured flexoelectric response were proposed for insulating ferroelectric ceramics. A barrier-layer theory was used to explain the large flexoelectric response in semiconductors [40,77,78]. In semiconductors, the depletion layers formed at the interfaces between the semiconductor and electrodes act as insulating barrier layers, providing an insulating environment for surface piezoelectricity [77]. Under bending, the surface piezoelectric response generates the flexoelectric-like response measured in semiconductors. Meanwhile, the middle semi-conducting region (bulk) separating the depletion layers acts as an intercalated electrode and provides free charges to respond to surface piezoelectricity, enhancing surface piezoelectricity (Figure 13) [77]. The enhanced surface piezoelectricity correspondingly contributes to the large flexoelectric-like response.
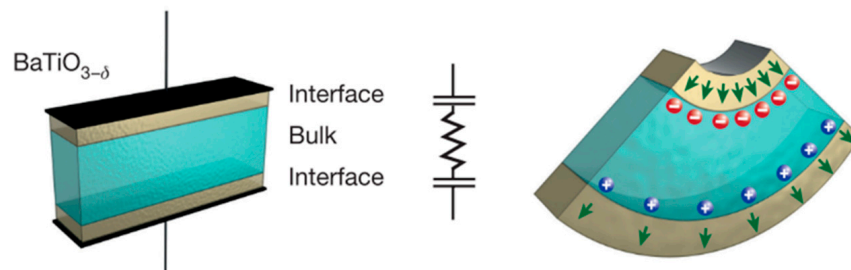
Figure 13. Schematic of a semiconductive $BaTiO_{3-\delta}$ crystal forming barrier layers on the surfaces, and the barrier layer theory enhancing surface piezoelectricity when bending the semiconductive $BaTiO_{3-\delta}$ crystal. Reprinted with permission from [77]. Copyright 2016 Springer Nature.

4.5. Other Theoretical Investigations

Besides the above theories, several other theories have also been proposed for the flexoelectric response of ferroelectric materials. Above the nominal T_C, it was found that

the flexoelectric coefficients of ferroelectric materials still deviate from the intrinsic values for BST ceramics and ferroelectricity still exists. Therefore, ferroelectricity was thought to be one of the origins of the flexoelectric response [79]. Interface effects, such as the interfaces between films and substrates, domain walls, or grain boundaries, generate an inhomogeneous strain and flexoelectric effect [22,80,81]. The piezoelectricity of grain boundaries is also a non-negligible factor [44]. In materials, compositional heterogeneity, which can induce structural heterogeneity, is a method used to enhance the flexoelectric response [55,61,82]. In addition, defects also influence the flexoelectric response [64,83]. For polymers, polymer chain motion, relaxation processes, and crystallinity affect the flexoelectric response [67,69].

## 5. Flexoelectric Scaling Effect in Nanoscale Materials

Equation (1) shows that the strain gradient also determines the flexoelectric response. The strain gradient depends on the applied forces, elastic modulus, and material dimensions. A large force is required for bulk materials to obtain a high strain gradient but the generated strain will surpass the upper strain limit above which the bulk materials will fracture [84]. For film materials, a large strain gradient is easy to produce using a low force due to their small dimensions, namely the flexoelectric scaling effect [38]. Especially for nanoscale materials, a small force can cause a huge strain gradient of $10^6 \sim 10^8$ m^{-1}, which is several orders of magnitude higher than that in bulk materials [7,9,13,82,85]. The strain gradient can be engineered by a lattice mismatch near the interface between the film and substrate, compositional gradient, sharp probes of atomic force microscopes, or bending nanoscale films and substrates (Figure 14) [6,82,85–94]. As shown in Figure 14a, the lattice mismatch between HoMnO$_3$ and the Pt(111)/Al$_2$O$_3$(0001) substrate can generate a large strain gradient of ~10^6 m^{-1} [93]. The strain gradient can be modulated by oxygen partial pressures, which control the distribution of oxygen vacancies in the oxide film (Figure 14b) [82]. Figure 14c shows that a giant strain gradient (up to >10^7 m^{-1}) can be produced through the sharp probe of an atomic force microscope compressing an ultrathin SrTiO$_3$ film [85]. Using the bending method shown in Figure 14d, the maximum strain gradient is ~0.5 m^{-1} due to the brittle nature of the single crystal substrate under a higher force [94]. The huge strain gradient induces a large flexoelectric field E_s, which is described by [13,82]:

$$E_s = \frac{e}{4\pi\varepsilon_0 a}\frac{\partial S}{\partial x} \tag{29}$$

In nanoscale materials, E_s can reach a magnitude of ~MV/m and trigger various physical phenomena, such as heightening piezoelectricity and polarization switching due to the flexoelectric effect [22,23,37,82,95–99]. In Figure 15, the piezoelectric response from the flexoelectric effect (measured using a cantilever) of the PZT and the BT films is enhanced as the thicknesses decrease [95]. The enhancement in the BT cantilever is much more pronounced than in the PZT cantilever in the ultrathin region (<10 nm) because of the high flexoelectric coefficient of BT (100× that of PZT). The piezoelectric response from the flexoelectric effect is different from the conventional piezoelectric response due to the differential production and origin, which is usually called the piezoelectric-like response. As shown in Figure 16, horizontal flexoelectricity forces the spontaneous polarization to rotate away from the normal to the horizonal plane in a ferroelectric film [97]. Apart from these common physical phenomena, many other surprising phenomena are attributable to the flexoelectric effect. It has been reported that E_s can manipulate the deformation and distribution of defects, the carrier density and mobility of two-dimensional electron gas (2DEG), the barrier of semiconductors, magnetoelectric responses, nanoindentation, thermal–electrical responses, driving triboelectricity, resistance and quantum tunneling of nanoscale dielectrics, photovoltage, and photocurrent, which are described in detail in the next section [85,89,90,92,94,100–110].
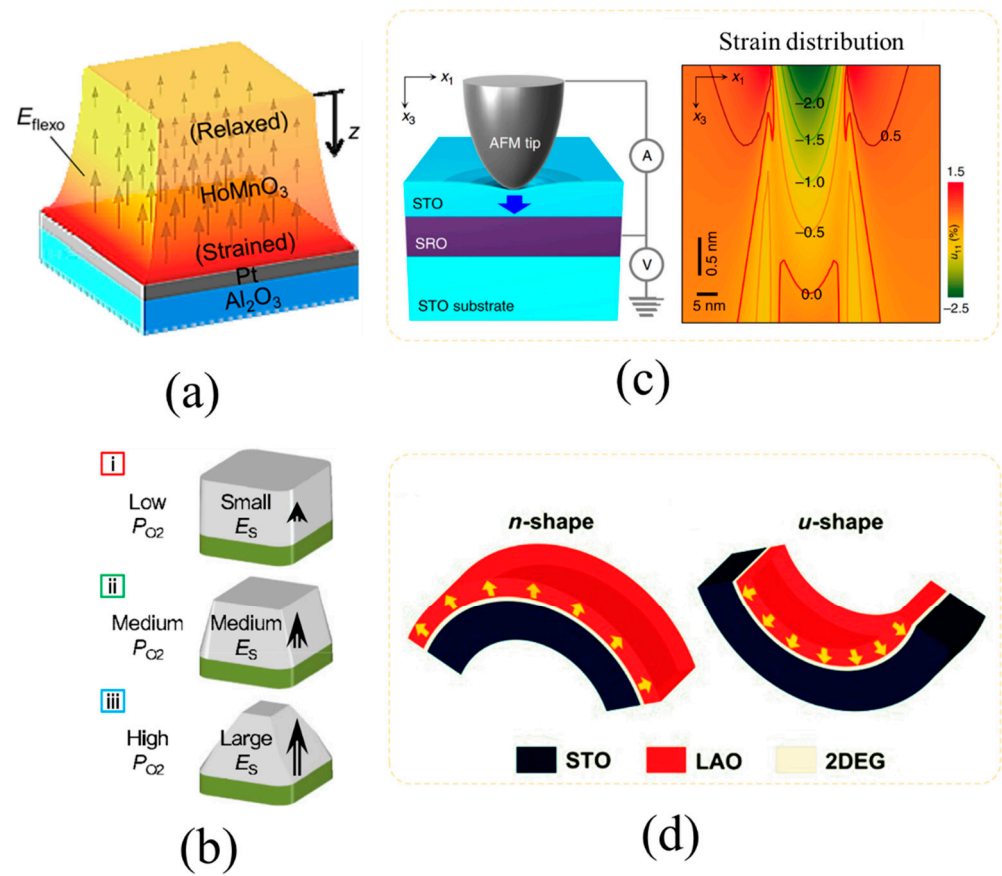
Figure 14. (**a**) The film generating a strain gradient through the interfacial lattice mismatch between the film and substrate Reprinted with permission from [93]. Copyright 2012 American Chemical Society. (**b**) Oxygen partial pressures controlling the oxygen vacancy gradient that modulates the strain gradient of the film. Reprinted with permission from [82]. Copyright 2011 American Physical Society. (**c**) The sharp probe of an atomic force microscope applying a compressive force to a film, causing strain gradient. Reprinted with permission from [85]. Copyright 2019 Springer Nature. (**d**) Bending films and substrates to obtain strain gradient. Reprinted with permission from [94]. Copyright 2019 American Physical Society.
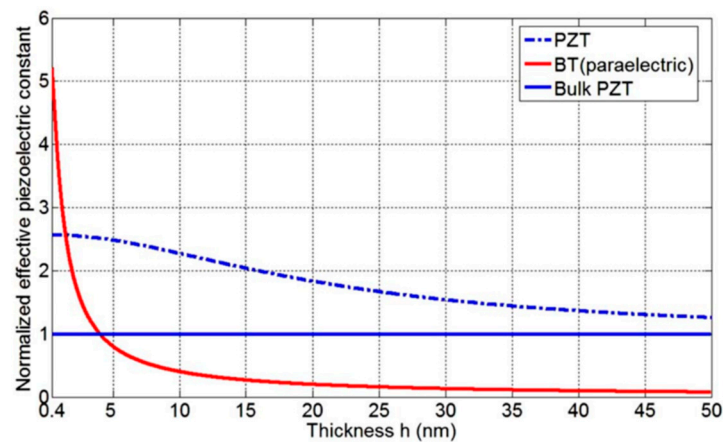
Figure 15. Effective piezoelectric constant of PZT (dashed blue line) and BT (solid red line) cantilevers. The piezoelectric constants of the two cantilevers are normalized with respect to the bulk PZT value (solid blue line). Reprinted with permission from [95]. Copyright 2008, American Physical Society).
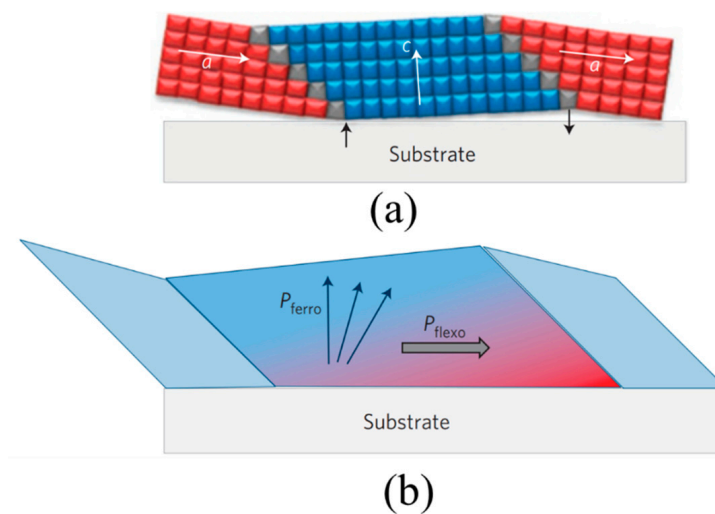
Figure 16. (**a**) Schematic representation of the domain structure in a film with a–c domains. The black arrows represent the stresses that must be applied to the twinned film to flatten it onto the substrate. (**b**) The flexoelectric polarization (grey) induces a rotation of the ferroelectric polarization of the c domain (blue). Reprinted with permission from [97]. Copyright 2011 Springer Nature.

6. Potential Applications of the Flexoelectric Effect

The flexoelectric effect has motivated several potential applications, such as flexoelectric piezoelectric composites, manipulation of ferroelectric polarization, energy conversion, sensors, and actuators, and several other progressive applications.

6.1. Flexoelectric Piezoelectric Composites

Conventional piezoelectricity only exists in non-centrosymmetric materials, which limits material selectivity. The flexoelectric effect artificially breaks material structural symmetry with geometrical asymmetry, which can generate a piezoelectric-like response. Cross et al. obtained a piezoelectric-like response of ~6 pC/N at room temperature by using $Ba_{0.67}Sr_{0.33}TiO_3$ (BST) ceramics (in the paraelectric phase) to design a 3×3 array of millimeter-scale square truncated pyramids, as shown in Figure 17a [111]. The piezoelectric-like response from the flexoelectric response mainly depends on the strain gradient due to the low flexoelectric coefficient in paraelectric materials. Furthermore, a flexure mode flexoelectric piezoelectric composite was designed, where fine tungsten wires were used to separate the BST ceramic sheets and compression stresses were applied to the top and bottom metal plates, causing bending of the ceramics and a high strain gradient, as illustrated in Figure 17b. As a result, a piezoelectric-like response of ~4300 pC/N was produced near T_C and maintained high values at higher temperatures (Figure 17c) [37]. To simplify the design, our research group designed a dome-like structure (Figure 17d) using the diffusion or asymmetrical reducing method [24,61]. The asymmetrical reducing method also causes a composition gradient [61]. Based on the asymmetrical reducing method, a piece of NBBT8 ceramic wafer can generate a high piezoelectric-like response of over 8000 pC/N measured using the point-ring method (Figure 8a) [60]. In addition, the bending Si crystal can also generate a piezoelectric-like response of ~80 pC/N for which the flexoelectric response is from the piezoelectric response of the surface oxide layers, and the high conductivity of the bulk and the bending deformation of the Si plates amplify the piezoelectric response [112]. It should be noted that the piezoelectric-like response from the flexoelectric response increases with decreasing the material thickness due to the flexoelectric scaling effect [23].
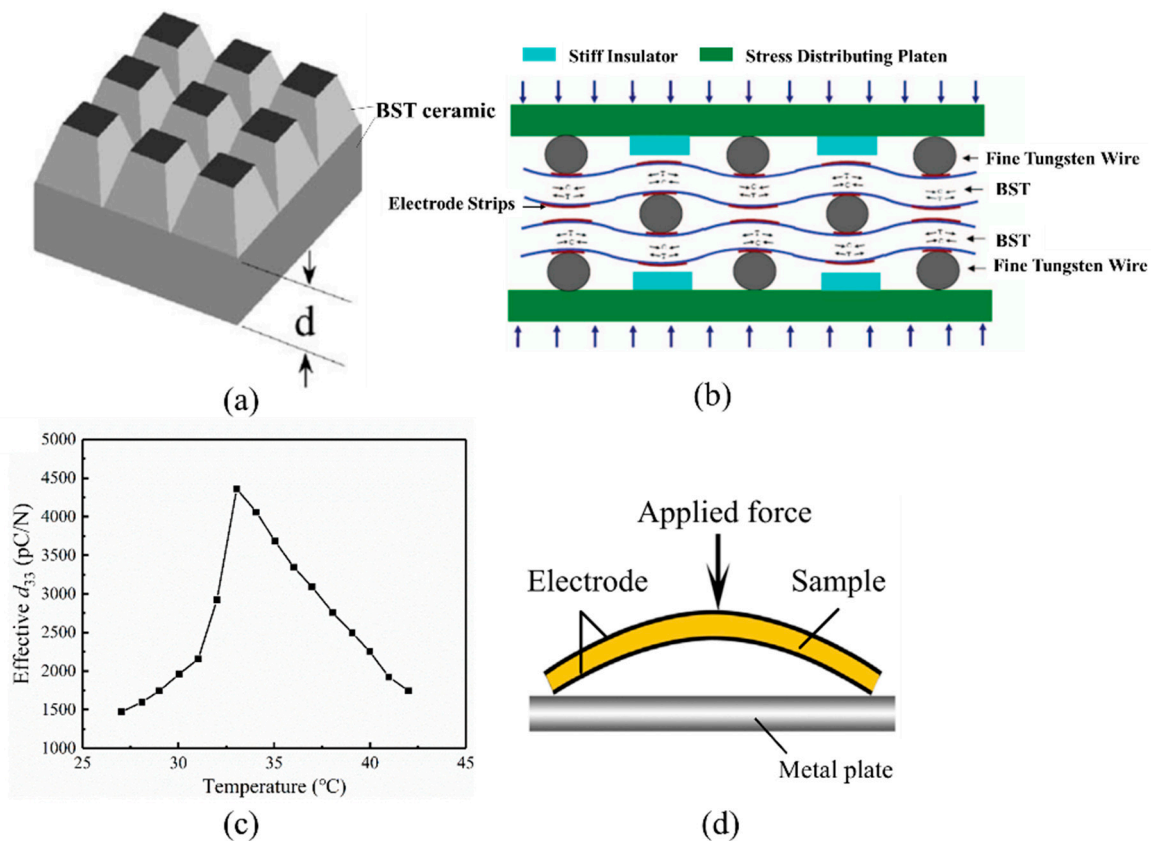
Figure 17. Schematic of (**a**) a 3 × 3 pyramid BST array structure (*d* = 0.52 mm) (reprinted with permission from [111]; copyright 2006 AIP Publishing) and (**b**) a flexure mode composite. (**c**) Effective d_{33} of three-layer six-unit BST composites. (**b**,**c**) Reprinted with permission from [37]. Copyright 2009 AIP Publishing). (**d**) A sample with a dome-like structure. Reprinted with permission from [24]. Copyright 2016 AIP Publishing.

6.2. Sensors and Actuators

　　Because of the sensitivity of the flexoelectric effect to stress or electric fields, the flexoelectric effect can also be used in the application of sensors and actuators [15,16,113,114]. Unlike the piezoelectric effect, the flexoelectric effect can still exist when the temperature exceeds T_d (the depolarization temperature). Thus, flexoelectric sensors and actuators can operate at higher temperatures [37]. Trapezoidal (Ba,Sr) TiO₃ ceramics were designed to be used in an acceleration sensor with a sensitivity of ~0.84 pC/g or a microphone with a sensitivity of ~0.85 pC/Pa and a signal to noise ratio of 74 dB utilizing the flexoelectric effect [115,116]. The asymmetrically reduced NBBT ceramics can induce a large displacement of ~17 μm by the converse flexoelectric effect (Figure 18a), which can be used in actuator applications [117]. When the size of materials decreases, the sensitivity of the sensors and actuators also increases due to the scaling effect of flexoelectricity. For example, the performance of SrTiO₃ film cantilever actuators can be comparable to that of Pb(Zr,Ti)O₃-based piezoelectric bimorphs (Figure 18b) [19].

6.3. Mechanical Writing

　　For materials with nanoscale sizes, the large strain gradient can induce a flexoelectric field E_s, which can exceed their coercive fields. As a result, E_s can manipulate domain switching, namely the stress controls the domains [82,97,98]. Figure 19 shows that the polarization and switching behavior of PZT films vary with the polarization orientation of the flexoelectric effect [98]. Based on these phenomena, a device with the function of mechanical writing was designed (Figure 20a,b) [74]. The strain gradient can be controlled by the size of the individual nanodots on polyvinylidene fluoride-trifluoroethylene (P(VDF-

TrFE)) to modulate E_s for the application of force-induced high-density data storage [99]. As shown in Figure 20c, from the letter "F" to the letter "E", the area of the individual nanodots becomes smaller, which is beneficial to the strain gradient, and the letters become clearer and have high signals [99].

(a)

(b)
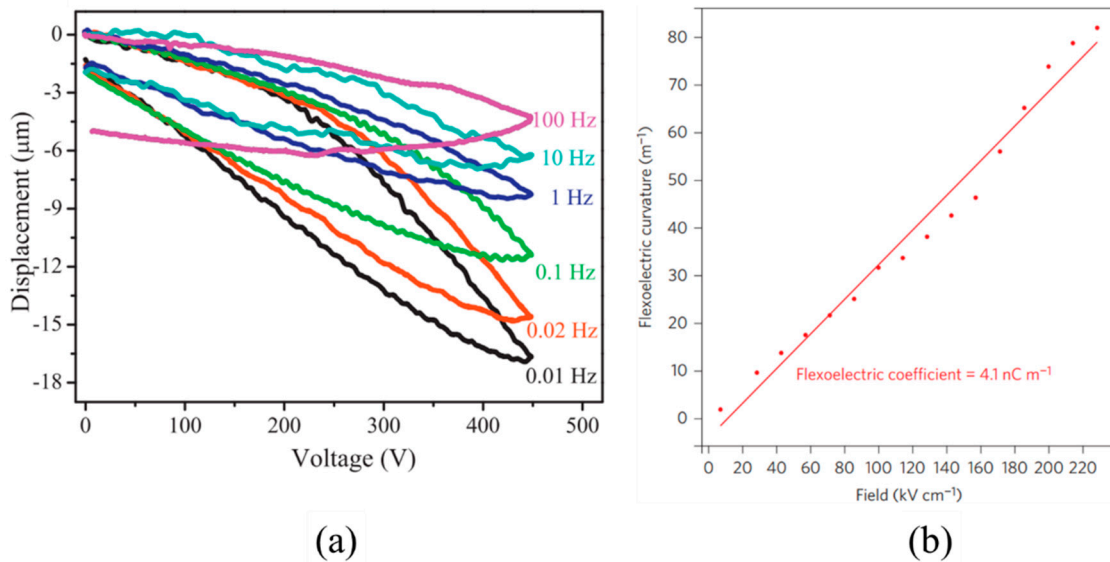
Figure 18. (**a**) Unipolar displacement of reduced NBBT8 ceramics under different voltages at different frequencies. Reprinted with permission from [117]. Copyright 2017 Elsevier. (**b**) The linear variance of the first-harmonic flexoelectric curvature with the applied ac field at a frequency of 100 kHz of MEMS actuators fabricated by SrTiO₃. Reprinted with permission from [19]. Copyright 2015 Springer Nature.
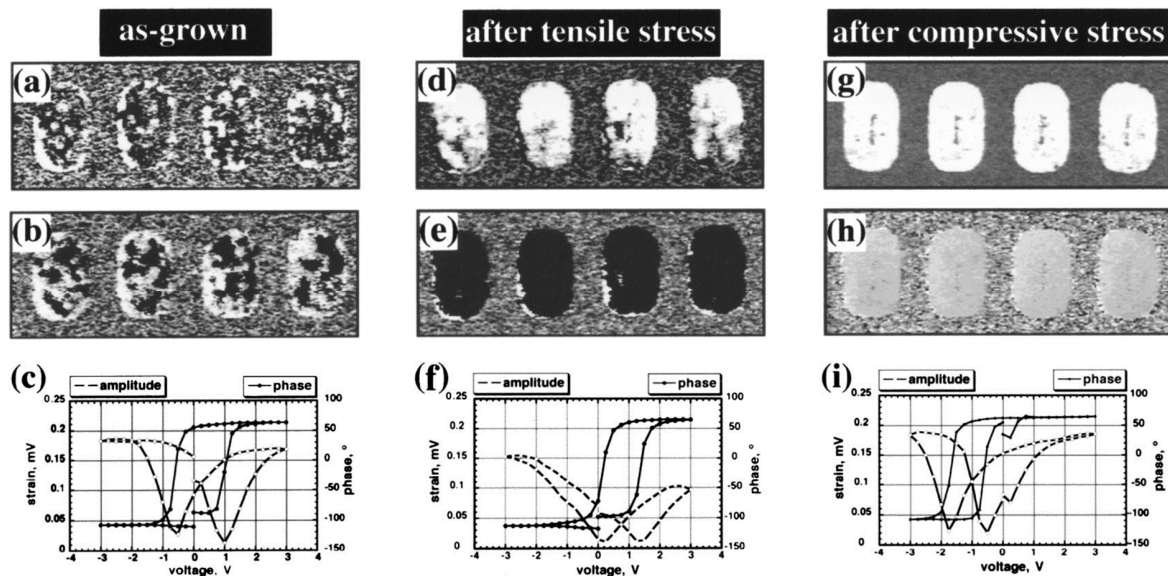
Figure 19. PFM images illustrating the impact of stress (generating the flexoelectric effect) on the polarization and switching behavior of (111)-oriented PZT capacitors. (**a–c**) Before applying stress: PFM amplitude (**a**) and phase (**b**) images of as-grown capacitors and a local hysteresis loop (**c**) measured near the edge of one of the capacitors. (**d–f**) After applying tensile stress: PFM amplitude (**d**) and phase (**e**) images of the same capacitors and a hysteresis loop (**f**) measured at the same site. (**g–i**) After applying compressive stress: PFM amplitude (**g**) and phase (**h**) images and a hysteresis loop (**i**) measured near the edge of one of the capacitors. Reprinted with permission from [98]. Copyright 2003 AIP Publishing.
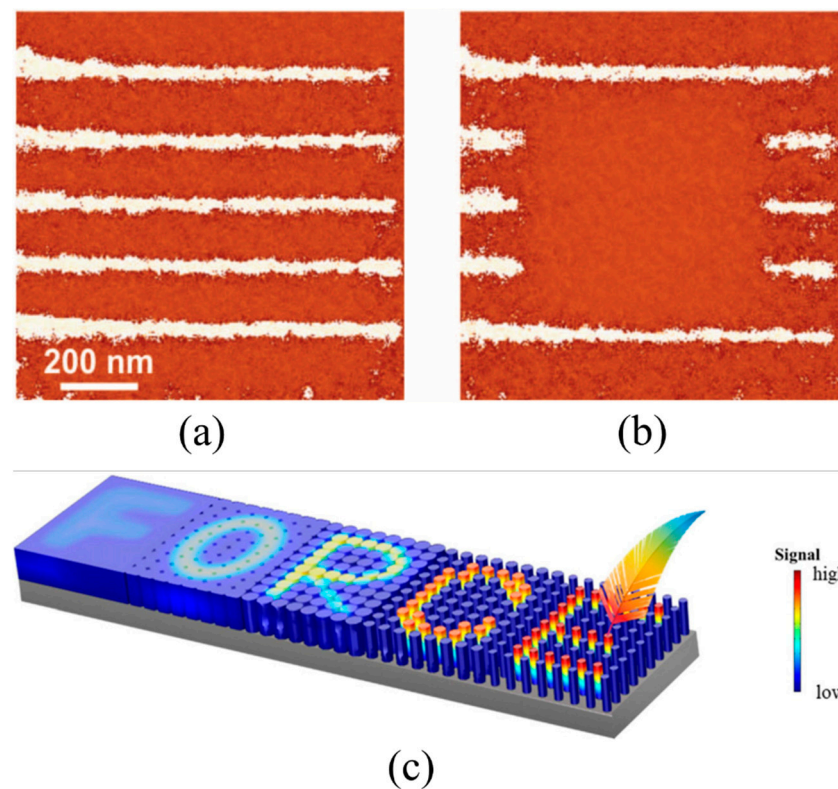
Figure 20. (**a**,**b**) Fabrication of nanoscale domain patterns using the tip of an atomic force microscope (AFM). Reprinted with permission from [74]. Copyright 2012 American Association for the Advancement of Science. (**a**) Domain lines were mechanically written on a $BaTiO_3$ film by scanning the film using the tip under a loading force of 1500 nN. (**b**) The same domain structure was modified by the electrical erasure of the mechanically written domains. The erasure was performed by scanning the central segment using the tip under a dc –3 V bias. (**c**) Scheme of the signal of force-induced devices on different surfaces with nanodots. Reprinted with permission from [99]. Copyright 2018 AIP Publishing.

6.4. Energy Harvester

Because the flexoelectric effect is the interconversion of mechanical and electrical energy, applications for converting mechanical energy to electrical energy have been developed [35,60,118]. Under bending, the reduced NBBT8 ceramics exhibit a large piezoelectric-like response, which can be used in mechanical energy-harvesting applications [60]. However, the energy-harvesting properties from the flexoelectric response are weaker than those of the conventional piezoelectric energy harvesters [60]. It is worth mentioning that the energy harvesting from the flexoelectric response can be maintained at a temperature higher than T_d (the temperature of the piezoelectric response disappearing in piezoelectric ceramics), as shown in Figure 21. To enhance the energy-harvesting properties, flexoelectric nanogenerators were designed due to the flexoelectric scaling effect [113,119].

The flexoelectric field E_s can also act as a driving electric field modulating carrier migration. At high temperatures, ferroelectric materials become more conductive and E_s can generate a thermal current [106]. This indicates that the flexoelectric effect can facilitate thermal energy harvesting (Figure 22) [106]. Furthermore, because the flexoelectric effect can provide a driving electric field, it implies that an uneven thermal environment, which is the driving force of conventional thermoelectricity, is not necessary for flexoelectric thermal energy harvesting. However, the conductivity of ferroelectric materials is lower than that of conventional thermoelectric materials, which limits the output thermal current. To enhance the conductivity, reduced ferroelectric ceramics and doping were adopted [107,120]. In addition, asymmetrically reduced ferroelectric ceramics can also improve E_s [107].

Consequently, a large power density of ~0.18 mW/cm^3 can be collected in the reduced NBBT8 ceramics at a temperature of 350 °C [107]. Thus, flexoelectric thermal energy harvesting depends mainly on the flexoelectric response and materials' conductivity. In addition, chemical inhomogeneities present in the asymmetrically reduced ferroelectric ceramics result in a built-in electric field [107].
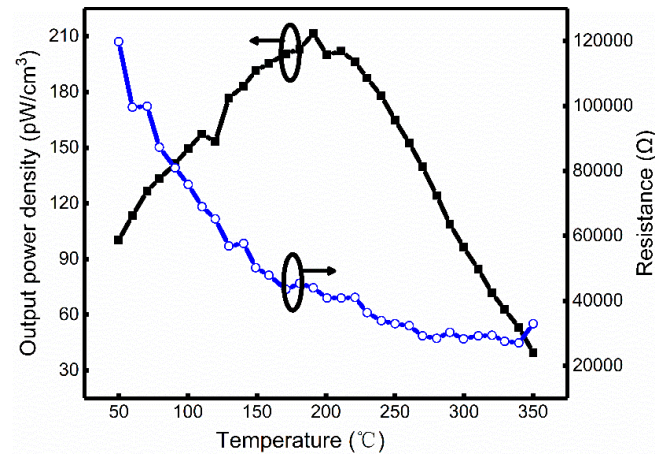

Figure 21. The temperature dependence of the output power density and the matched resistance measured in the unreduced NBBT8 ceramics. Reprinted with permission from [60]. Copyright 2018 Elsevier. T_d is ~140 °C for the NBBT8 ceramics.


(a)　　(b)
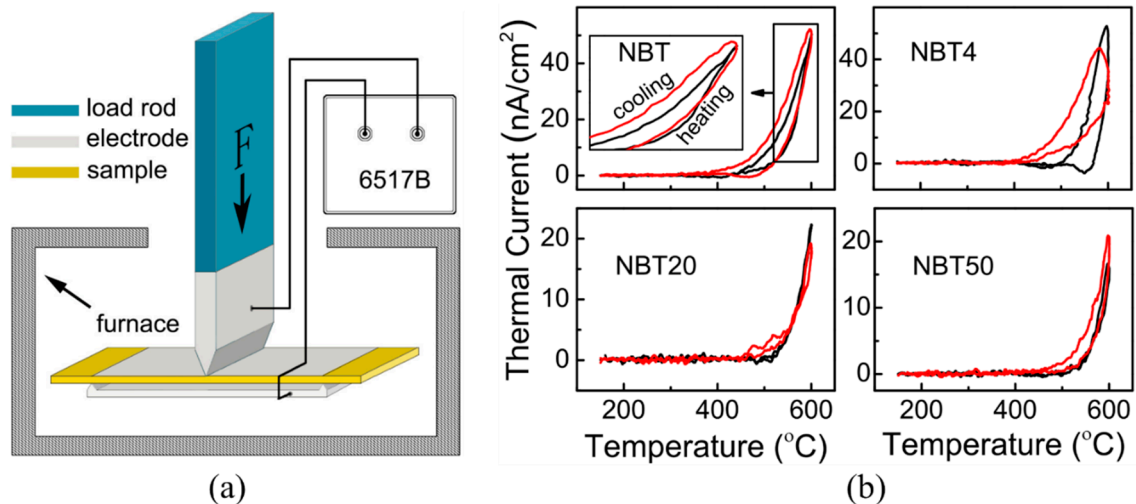
Figure 22. (**a**) Schematic of the thermal current measurements under the application of a three-point bending load to the samples. (**b**) The temperature dependence of the thermal current density of BNT-based ceramic plates using the test device in (**a**). The red curves are the measured results after flipping the samples. The current direction is mainly dependent on the direction of the strain gradient, which is less related to the direction of the heat transfer. Reprinted with permission from [106]. Copyright 2018 American Physical Society.

The flexoelectric effect can also be involved in photoelectric conversion. Similar to the bulk photovoltaic effect of ferroelectric materials in which the absence of structural symmetry causes the asymmetric distribution of photoexcited non-equilibrium carriers in momentum space, the flexoelectric effect breaks the center symmetry of the structure to generate photoexcited non-equilibrium carriers in centrosymmetric materials, such as single crystals of $SrTiO_3$, TiO_2, and Si [104]. The bulk photovoltaic effect caused by the flexoelectric effect is called the flexo-photovoltaic effect (Figure 23). For low-dimensional materials, larger strain gradients render a stronger flexo-photovoltaic effect [105,121,122].

Recently, another photoelectric conversion phenomenon in which light can modulate the flexoelectric-like response of semiconductors was reported, which was defined as the photo-flexoelectric effect (Figure 24) [78]. Given the barrier-layer theory of the flexoelectric-like response of semiconductors, light tunes the Schottky barrier height to control the free carriers compensating for the surface piezoelectricity [78]. The photo-flexoelectric effect can be further enhanced when oxygen vacancies induce defect levels as light absorption centers, which convert photon energy to electron–hole pairs [123].

(a)   (b)
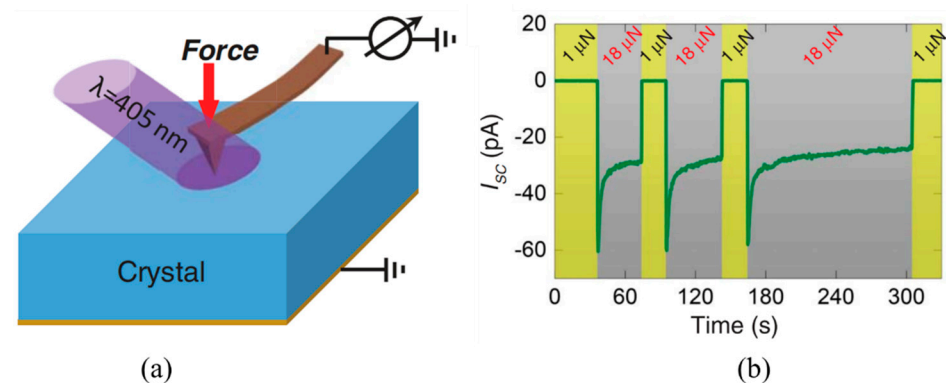
Figure 23. (**a**) Schematic of the AFM tip applying a load to generate a strain gradient in an illuminating area of dielectrics. (**b**) Evolution of the photocurrent from the flexoelectric response with forces for SrTiO$_3$ single crystals. Reprinted with permission from [104]. Copyright 2018 American Association for the Advancement of Science.
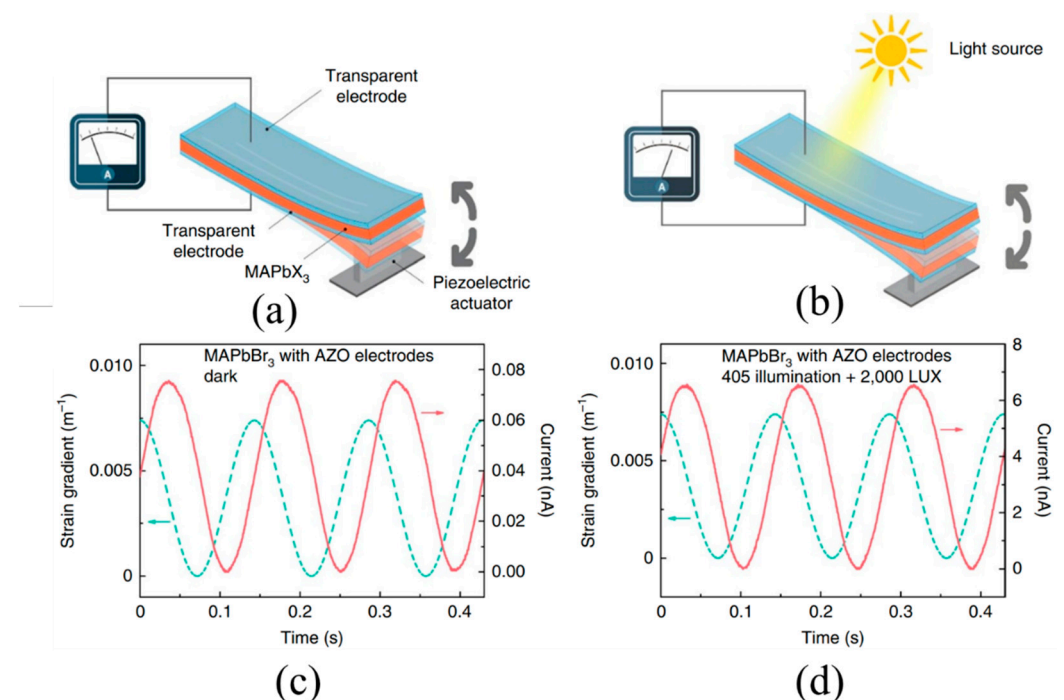

Figure 24. Cantilever bending the halide capacitors (where X is Cl, Br, or I) with transparent electrodes in the dark (**a**) or under light (**b**). The evolution of the collected current and strain gradient with time in the dark (**c**) or under light (**d**). Reprinted with permission from [78]. Copyright 2020 Springer Nature.

6.5. Other Applications

The flexoelectric effect can reconfigure the distribution of oxygen vacancies, as shown in Figure 25 [101]. The strain gradient of STO film was produced using the spherical tip of a Kelvin probe force microscope to compress the grey boxes, as shown in Figure 25a [101]. In the grey boxes in Figure 25a, the change in the normalized vacancy concentration (NVC)

along lines M1, M2, M3, and M4 (Figure 25b) indicates that the flexoelectric effect affects the concentration of oxygen vacancies [101]. In semiconductors, the flexoelectric effect can be used to manipulate the barrier height, maximum rectified current density, reverse saturation current density, maximum rectified ratio, and open voltage of Schottky barrier diodes (Figure 26) [90]. Utilizing mechanical touching or rubbing to generate a strain gradient, the flexoelectric effect has a non-negligible effect on the peak-to-peak voltage of triboelectric devices (Figure 27) [124]. The flexoelectric effect plays the role of a built-in electric field and can be utilized to generate a rectifying diode effect [93,107]. As shown in Figure 28a, the relationship between the current density and electrical field exhibits a rectifying diode effect for asymmetrically reduced NBBT8 ceramics [107]. Furthermore, in ultrathin dielectrics, Noh et al. reported that the flexoelectric effect controls quantum tunneling or resistance through strain gradients by modifying the band structure of ultrathin dielectrics (Figure 28c) [85,89]. Dai et al. bent $LaAlO_3$ to control the electrical transport properties of the interfacial 2DEG at the $LaAlO_3/SrTiO_3$ heterostructure (Figure 28b) [94]. In inhomogeneous ferromagnetic materials, the inhomogeneous magnetostrictive response generates bending deformation and a flexoelectric effect, inducing a magnetoelectric response (Figure 29) [62]. Through a strain gradient, a topologically flexomagnetic response can be enhanced in synthetic antiferromagnetic systems hosting skyrmions, and the systems exhibit a flexo-Hall effect [125].
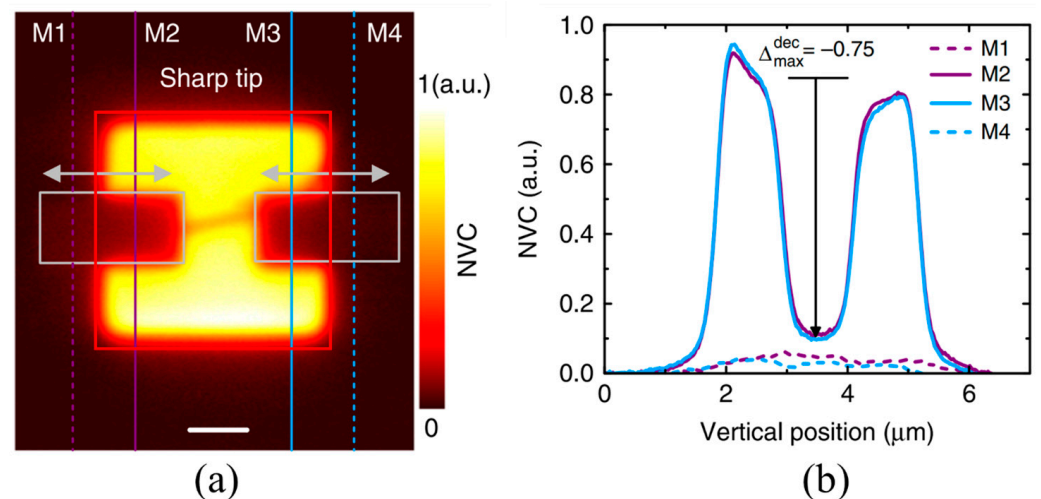
Figure 25. Controlled manipulation of oxygen vacancies. (**a**) The normalized vacancy concentration (NVC) maps after mechanical scans were performed using a sharp tip with a contact force of 9.5 µN within the grey boxes. Horizontal arrows indicate the corresponding fast scan direction. (**b**) NVC profiles along lines M1, M2, M3, and M4. M1 and M4 are placed 0.5 µm away from the borders between the $V_O^{\cdot\cdot}$-enriched region (inside the red box) and the pristine region (outside the red box). Horizontal black lines in (**b**) indicate the background, which is used to estimate the net change in the NVC. The NVC profiles were averaged over a 0.5 µm wide averaging window. Reprinted with permission from [101]. Copyright 2020 Springer Nature.
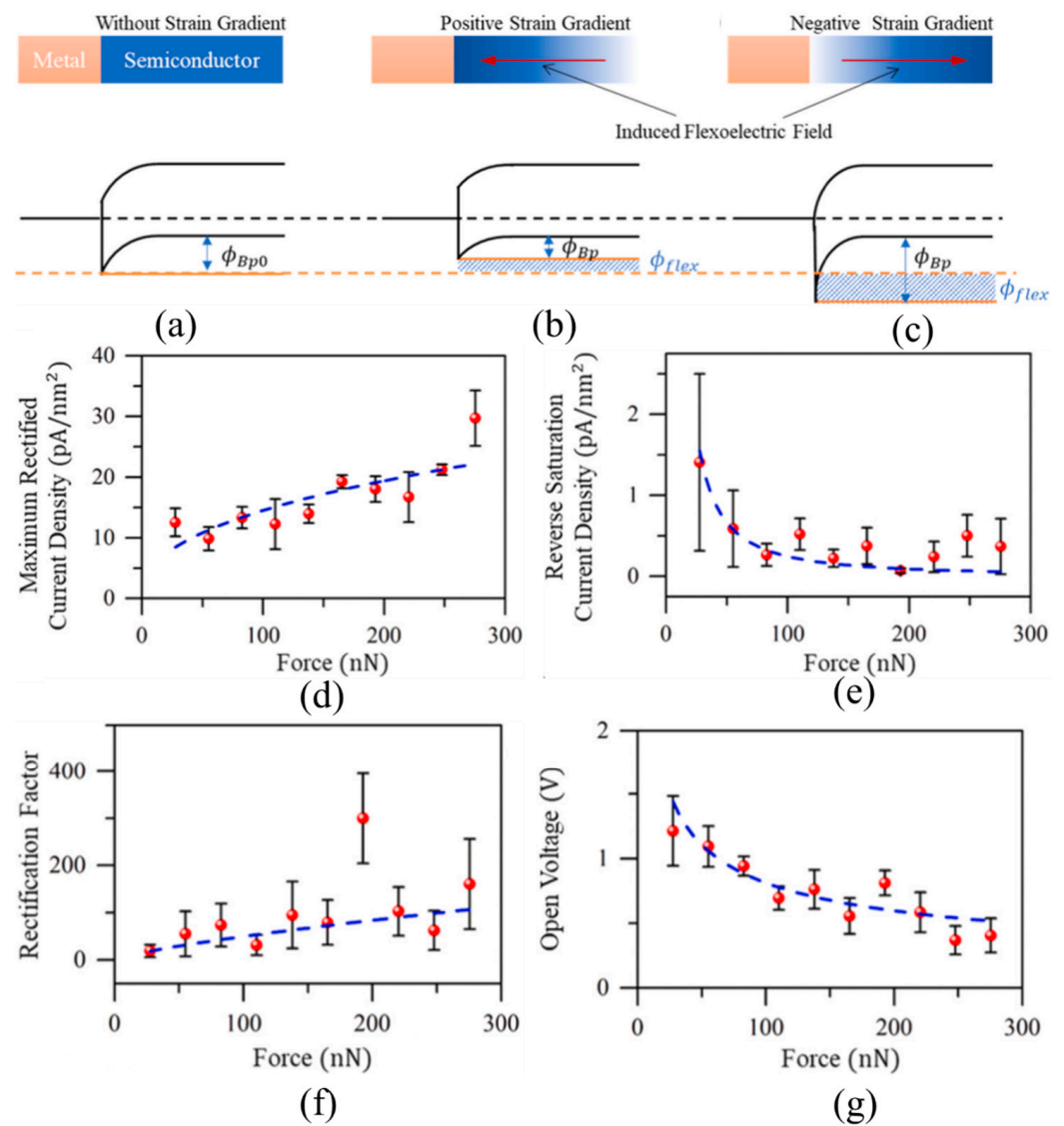
Figure 26. Energy band diagram of metal-Si (p-type) contact under (**a**) no strain gradient, (**b**) positive strain gradient, and (**c**) negative strain gradient. The effect of the induced flexoelectric polarization on the (**d**) maximum rectified current density, (**e**) reverse saturation current density, (**f**) rectification ratio, and (**g**) open voltage for silicon-based Schottky barrier diode devices. The red dots are the experimental results and the blue dotted lines are their fitted curves. Reprinted with permission from [90]. Copyright 2021 Elsevier.
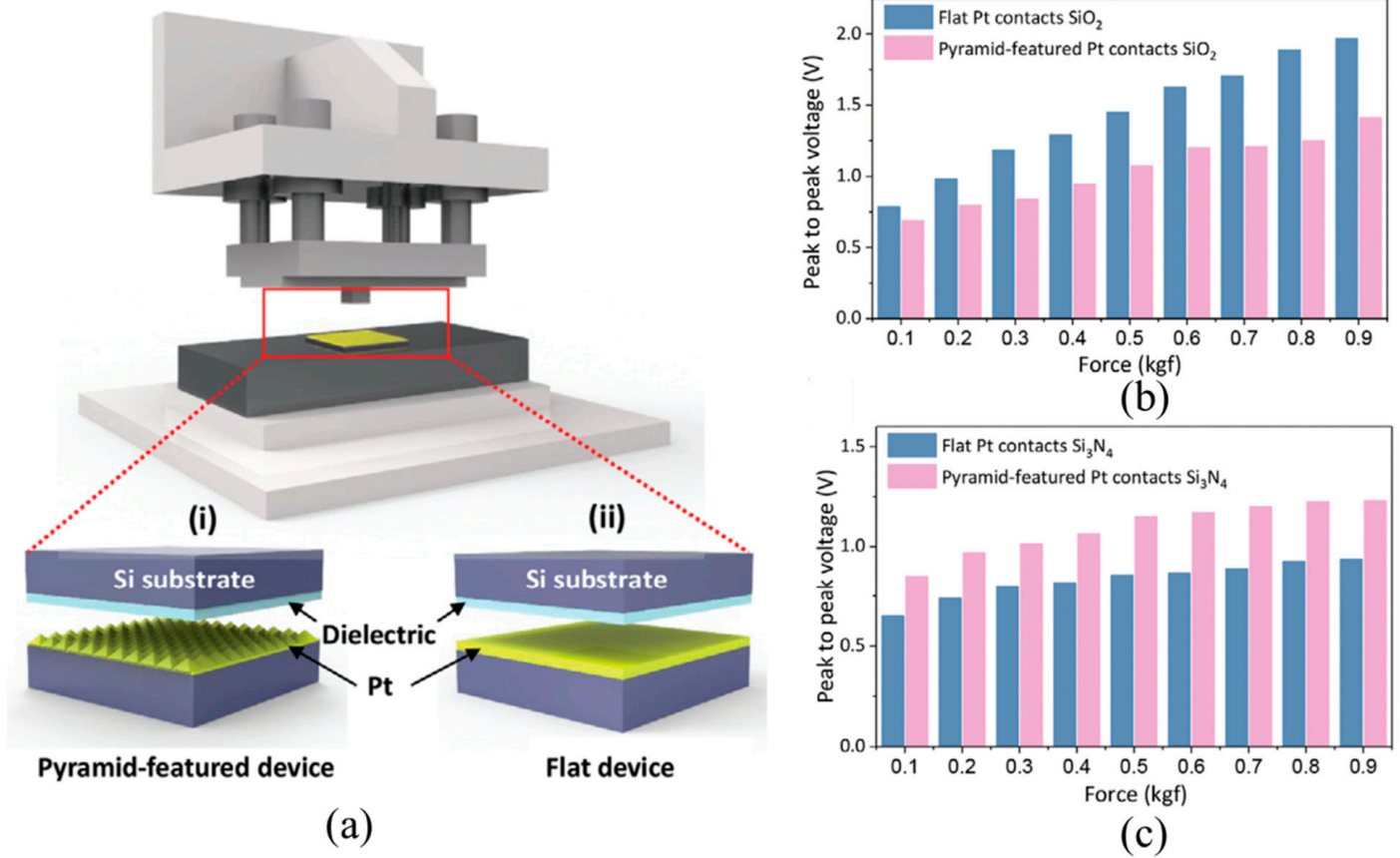
Figure 27. (**a**) Schematic diagrams of triboelectric devices: (i) pyramid-featured Pt (generating strain gradient on dielectric films) and (ii) flat Pt. (**b**,**c**) Peak-to-peak voltage as a function of the applied force (1 kgf = 9.8 N) in triboelectric devices of flat Pt and pyramid-featured Pt contact (**b**) SiO_2 and (**c**) Si_3N_4 thin films. For pyramid-featured Pt and SiO_2, the triboelectric effect is suppressed by the flexoelectric effect owing to opposite charge transfer directions, which leads to a smaller peak-to-peak voltage in the pyramid-featured device than in the flat device. For pyramid-featured Pt and Si_3N_4, the triboelectric effect is improved by the flexoelectric effect owing to uniform charge transfer directions, which leads to a larger peak-to-peak voltage in the pyramid-featured device than in the flat device. Reprinted with permission from [124]. Copyright 2021 Wiley.
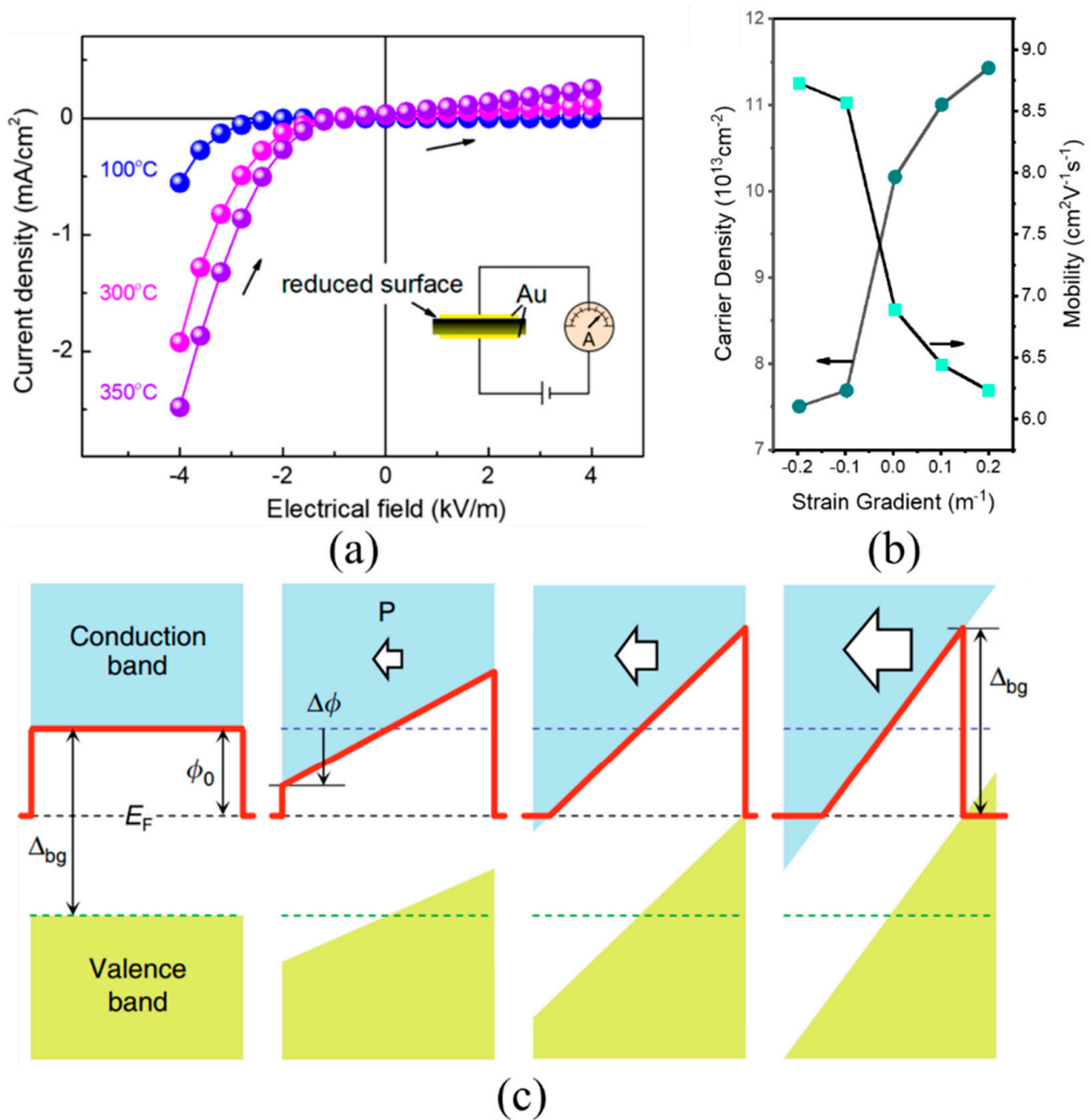
Figure 28. (**a**) The rectifying diode effect in asymmetrically reduced NBT-based ferroelectric ceramics because of the built-in electric field from the flexoelectric effect. Reprinted with permission from [107]. Copyright 2019 American Chemical Society. (**b**) The interface carrier densities and mobilities of 2DEG under different strain gradients for the $LaAlO_3/SrTiO_3$ heterostructure. Reprinted with permission from [94]. Copyright 2019 American Physical Society. (**c**) Schematic diagram of the potential energy profiles with increasing flexoelectric polarization P (white arrow). The solid red and black dashed lines indicate the effective tunnel barrier and the Fermi level, respectively. The blue and green dashed lines indicate the conduction band minimum and valence band maximum for $P = 0$, respectively. Reprinted with permission from [89]. Copyright 2020 Springer Nature.
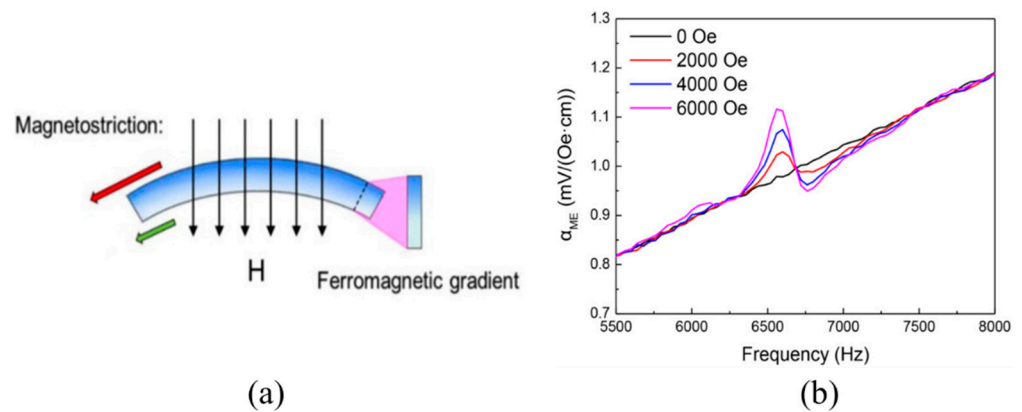
Figure 29. (**a**) A schematic illustration of the magnetic field-induced bending of the inhomogeneously reduced BFO-BTO ceramic wafers due to the inhomogeneous magnetostrictive response across the thickness. The bending causes a flexoelectric response. (**b**) The effect of the DC magnetic field on the magnetoelectric coupling coefficient for the BFO-BTO ceramics. The electric voltage is from the flexoelectric response. Reprinted with permission from [62]. Copyright 2019 Elsevier.

7. Summary and Future Trends

This review summarizes the reported experimental results of flexoelectricity in ferroelectric materials. Different measurement methods have been designed for flexoelectric coefficients, but a technique to separate the non-zero components of the flexoelectric coefficients of ferroelectric materials is still missing. As seen from the reported flexoelectric coefficients, they are several orders of magnitude larger than the theoretical values for ferroelectric materials. Although the spontaneously polarized surface theory can largely explain this issue, other theories may also contribute to the measured flexoelectric coefficients. Therefore, further research is necessary to fully understand the origin of the large flexoelectric response observed in ferroelectric ceramics.

For the applications of flexoelectric response, the criteria for achieving better performance are a large flexoelectric coefficient and strain gradient. Thus, enhancing the flexoelectric coefficient and strain gradient is necessary. A common approach to increasing strain gradients is to reduce the size of materials, for example, by fabricating nanoscale films. However, obtaining a large strain gradient in bulk materials is still difficult. Reducing the size of materials to nanoscale is in line with the development of small electronic devices. Because of the universality of flexoelectric response, strain gradients have been demonstrated to affect many physical properties through the generation of a flexoelectric field, which is an interdisciplinary research direction.

Author Contributions: D.T. conceptualized the framework for this paper, collected the data, and wrote the sections on the innovation of components. D.-Y.J. oversaw and edited this paper. Z.F. contributed to the aforementioned sections. B.C. conceptualized the framework for this paper and contributed to the aforementioned sections. All authors have read and agreed to the published version of the manuscript.

Data Availability Statement: Not applicable.

Conflicts of Interest: The authors declare no conflict of interest.

References

1. Cross, L.E. Flexoelectric effects: Charge separation in insulating solids subjected to elastic strain gradients. *J. Mater. Sci.* **2006**, *41*, 53–63. [CrossRef]
2. Quang, H.L.; He, Q.C. The number and types of all possible rotational symmetries for flexoelectric tensors. *Proc. R. Soc. A Math. Phys. Eng. Sci.* **2011**, *467*, 2369–2386. [CrossRef]
3. Shu, L.; Wei, X.; Pang, T.; Yao, X.; Wang, C. Symmetry of flexoelectric coefficients in crystalline medium. *J. Appl. Phys.* **2011**, *110*, 104106. [CrossRef]
4. Yudin, P.V.; Tagantsev, A.K. Fundamentals of flexoelectricity in solids. *Nanotechnology* **2013**, *24*, 432001. [CrossRef] [PubMed]
5. Tagantsev, A.K. Electric polarization in crystals and its response to thermal and elastic perturbations. *Phase Trans.* **1991**, *35*, 119–203. [CrossRef]
6. Zubko, P.; Catalan, G.; Tagantsev, A.K. Flexoelectric Effect in Solids. *Annu. Rev. Mater. Res.* **2013**, *43*, 387–421. [CrossRef]
7. Ma, W.; Cross, L.E. Observation of the flexoelectric effect in relaxor $Pb(Mg_{1/3}Nb_{2/3})O_3$ ceramics. *Appl. Phys. Lett.* **2001**, *78*, 2920–2921. [CrossRef]
8. Ma, W.; Cross, L.E. Large flexoelectric polarization in ceramic lead magnesium niobate. *Appl. Phys. Lett.* **2001**, *79*, 4420–4422. [CrossRef]
9. Ma, W.; Cross, L.E. Flexoelectric polarization of barium strontium titanate in the paraelectric state. *Appl. Phys. Lett.* **2002**, *81*, 3440–3442. [CrossRef]
10. Ma, W.; Cross, L.E. Strain-gradient-induced electric polarization in lead zirconate titanate ceramics. *Appl. Phys. Lett.* **2003**, *82*, 3293–3295. [CrossRef]
11. Zhou, W.; Chen, P.; Chu, B. Flexoelectricity in ferroelectric materials. *IET Nanodielectr.* **2019**, *2*, 83–91. [CrossRef]
12. Wang, B.; Gu, Y.; Zhang, S.; Chen, L.-Q. Flexoelectricity in solids: Progress, challenges, and perspectives. *Prog. Mater. Sci.* **2019**, *106*, 100570. [CrossRef]
13. Nguyen, T.D.; Mao, S.; Yeh, Y.W.; Purohit, P.K.; McAlpine, M.C. Nanoscale flexoelectricity. *Adv. Mater.* **2013**, *25*, 946–974. [CrossRef]
14. Deng, Q.; Kammoun, M.; Erturk, A.; Sharma, P. Nanoscale flexoelectric energy harvesting. *Int. J. Solids Struct.* **2014**, *51*, 3218–3225. [CrossRef]
15. Shu, L.; Liang, R.; Rao, Z.; Fei, L.; Ke, S.; Wang, Y. Flexoelectric materials and their related applications: A focused review. *J. Adv. Ceram.* **2019**, *8*, 153–173. [CrossRef]
16. Tripathy, A.; Saravanakumar, B.; Mohanty, S.; Nayak, S.K.; Ramadoss, A. Comprehensive Review on Flexoelectric Energy Harvesting Technology: Mechanisms, Device Configurations, and Potential Applications. *ACS Appl. Electron. Mater.* **2021**, *3*, 2898–2924. [CrossRef]
17. Kwon, S.R.; Huang, W.B.; Zhang, S.J.; Yuan, F.G.; Jiang, X.N. Flexoelectric sensing using a multilayered barium strontium titanate structure. *Smart Mater. Struct.* **2013**, *22*, 115017. [CrossRef]
18. Yan, X.; Huang, W.; Ryung Kwon, S.; Yang, S.; Jiang, X.; Yuan, F.-G. A sensor for the direct measurement of curvature based on flexoelectricity. *Smart Mater. Struct.* **2013**, *22*, 085016. [CrossRef]
19. Bhaskar, U.K.; Banerjee, N.; Abdollahi, A.; Wang, Z.; Schlom, D.G.; Rijnders, G.; Catalan, G. A flexoelectric microelectromechanical system on silicon. *Nat. Nanotechnol.* **2016**, *11*, 263–266. [CrossRef]
20. Wang, K.F.; Wang, B.L. Non-linear flexoelectricity in energy harvesting. *Int. J. Eng. Sci.* **2017**, *116*, 88–103. [CrossRef]
21. Chu, B.; Salem, D.R. Flexoelectricity in several thermoplastic and thermosetting polymers. *Appl. Phys. Lett.* **2012**, *101*, 103905. [CrossRef]
22. Zubko, P.; Catalan, G.; Buckley, A.; Welche, P.R.; Scott, J.F. Strain-gradient-induced polarization in $SrTiO_3$ single crystals. *Phys. Rev. Lett.* **2007**, *99*, 167601. [CrossRef] [PubMed]
23. Chu, B.; Zhu, W.; Li, N.A.N.; Cross, L.E. Flexoelectric Composite—A New Prospect for Lead-Free Piezoelectrics. *Funct. Mater. Lett.* **2011**, *03*, 79–81. [CrossRef]
24. Zhang, X.; Liu, J.; Chu, M.; Chu, B. Flexoelectric piezoelectric metamaterials based on the bending of ferroelectric ceramic wafers. *Appl. Phys. Lett.* **2016**, *109*, 072903. [CrossRef]
25. Abdollahi, A.; Millán, D.; Peco, C.; Arroyo, M.; Arias, I. Revisiting pyramid compression to quantify flexoelectricity: A three-dimensional simulation study. *Phys. Rev. B* **2015**, *91*, 104103. [CrossRef]
26. Lu, J.; Lv, J.; Liang, X.; Xu, M.; Shen, S. Improved approach to measure the direct flexoelectric coefficient of bulk polyvinylidene fluoride. *J. Appl. Phys.* **2016**, *119*, 094104. [CrossRef]
27. Biancoli, A.; Fancher, C.M.; Jones, J.L.; Damjanovic, D. Breaking of macroscopic centric symmetry in paraelectric phases of ferroelectric materials and implications for flexoelectricity. *Nat. Mater.* **2015**, *14*, 224–229. [CrossRef]
28. Baskaran, S.; Ramachandran, N.; He, X.; Thiruvannamalai, S.; Lee, H.J.; Heo, H.; Chen, Q.; Fu, J.Y. Giant flexoelectricity in polyvinylidene fluoride films. *Phys. Lett. A* **2011**, *375*, 2082–2084. [CrossRef]
29. Baskaran, S.; He, X.; Chen, Q.; Fu, J.Y. Experimental studies on the direct flexoelectric effect in α-phase polyvinylidene fluoride films. *Appl. Phys. Lett.* **2011**, *98*, 242901. [CrossRef]
30. Hu, T.; Deng, Q.; Liang, X.; Shen, S. Measuring the flexoelectric coefficient of bulk barium titanate from a shock wave experiment. *J. Appl. Phys.* **2017**, *122*, 055106. [CrossRef]

31. Zhang, S.; Xu, M.; Liang, X.; Shen, S. Shear flexoelectric coefficient μ_{1211} in polyvinylidene fluoride. *J. Appl. Phys.* **2015**, *117*, 204102. [CrossRef]

32. Zhang, S.; Liang, X.; Xu, M.; Feng, B.; Shen, S. Shear flexoelectric response along 3121 direction in polyvinylidene fluoride. *Appl. Phys. Lett.* **2015**, *107*, 142902. [CrossRef]

33. Fu, J.Y.; Zhu, W.; Li, N.; Cross, L.E. Experimental studies of the converse flexoelectric effect induced by inhomogeneous electric field in a barium strontium titanate composition. *J. Appl. Phys.* **2006**, *100*, 024112. [CrossRef]

34. Shu, L.; Huang, W.; Ryung Kwon, S.; Wang, Z.; Li, F.; Wei, X.; Zhang, S.; Lanagan, M.; Yao, X.; Jiang, X. Converse flexoelectric coefficient f_{1212} in bulk $Ba_{0.67}Sr_{0.33}TiO_3$. *Appl. Phys. Lett.* **2014**, *104*, 232902. [CrossRef]

35. Xia, Y.; Ji, Y.; Liu, Y.; Wu, L.; Yang, Y. Controllable Piezo-flexoelectric Effect in Ferroelectric $Ba_{0.7}Sr_{0.3}TiO_3$ Materials for Harvesting Vibration Energy. *ACS Appl. Mater. Interfaces* **2022**, *14*, 36763–36770. [CrossRef]

36. Hou, Y.; Tian, D.; Chu, B. Flexoelectric response of $(1-x)BaTiO_3$-$xSrTiO_3$ ceramics. *Ceram. Int.* **2020**, *46*, 12928–12932. [CrossRef]

37. Chu, B.; Zhu, W.; Li, N.; Cross, L.E. Flexure mode flexoelectric piezoelectric composites. *J. Appl. Phys.* **2009**, *106*, 104109. [CrossRef]

38. Huang, W.; Kim, K.; Zhang, S.; Yuan, F.-G.; Jiang, X. Scaling effect of flexoelectric (Ba,Sr)TiO_3 microcantilevers. *Phys. Status Solidi RRL* **2011**, *5*, 350–352. [CrossRef]

39. Li, Y.; Shu, L.; Huang, W.; Jiang, X.; Wang, H. Giant flexoelectricity in $Ba_{0.6}Sr_{0.4}TiO_3/Ni_{0.8}Zn_{0.2}Fe_2O_4$ composite. *Appl. Phys. Lett.* **2014**, *105*, 162906. [CrossRef]

40. Dai, Z.; Guo, S.; Gong, Y.; Wang, Z. Semiconductor flexoelectricity in graphite-doped $SrTiO_3$ ceramics. *Ceram. Int.* **2021**, *47*, 6535–6539. [CrossRef]

41. Mizzi, C.A.; Guo, B.; Marks, L.D. Experimental determination of flexoelectric coefficients in $SrTiO_3$, $KTaO_3$, TiO_2, and $YAlO_3$ single crystals. *Phys. Rev. Mater.* **2022**, *6*, 055005. [CrossRef]

42. Tian, D.; Hou, Y.; Zhou, W.; Chu, B. Flexoelectric response of ferroelectric ceramics with reduced surface layer effect. *J. Appl. Phys.* **2021**, *129*, 194103. [CrossRef]

43. Ma, W.; Cross, L.E. Flexoelectricity of barium titanate. *Appl. Phys. Lett.* **2006**, *88*, 232902. [CrossRef]

44. Narvaez, J.; Saremi, S.; Hong, J.; Stengel, M.; Catalan, G. Large Flexoelectric Anisotropy in Paraelectric Barium Titanate. *Phys. Rev. Lett.* **2015**, *115*, 037601. [CrossRef]

45. Zhang, X.; Pan, Q.; Tian, D.; Zhou, W.; Chen, P.; Zhang, H.; Chu, B. Large Flexoelectriclike Response from the Spontaneously Polarized Surfaces in Ferroelectric Ceramics. *Phys. Rev. Lett.* **2018**, *121*, 057602. [CrossRef] [PubMed]

46. Huang, S.; Kim, T.; Hou, D.; Cann, D.; Jones, J.L.; Jiang, X. Flexoelectric characterization of $BaTiO_3$-$0.08Bi(Zn_{1/2}Ti_{1/2})O_3$. *Appl. Phys. Lett.* **2017**, *110*, 222904. [CrossRef]

47. Shu, L.; Wei, X.; Jin, L.; Li, Y.; Wang, H.; Yao, X. Enhanced direct flexoelectricity in paraelectric phase of $Ba(Ti_{0.87}Sn_{0.13})O_3$ ceramics. *Appl. Phys. Lett.* **2013**, *102*, 152904. [CrossRef]

48. Shu, L.; Wan, M.; Wang, Z.; Wang, L.; Lei, S.; Wang, T.; Huang, W.; Zhou, N.; Wang, Y. Large flexoelectricity in Al_2O_3-doped $Ba(Ti_{0.85}Sn_{0.15})O_3$ ceramics. *Appl. Phys. Lett.* **2017**, *110*, 192903. [CrossRef]

49. Hana, P. Study of Flexoelectric Phenomenon from Direct and from Inverse Flexoelectric Behavior of PMNT Ceramic. *Ferroelectrics* **2007**, *351*, 196–203. [CrossRef]

50. Hana, P.; Marvan, M.; Burianova, L.; Zhang, S.J.; Furman, E.; Shrout, T.R. Study of the Inverse Flexoelectric Phenomena in Ceramic Lead Magnesium Niobate-Lead Titanate. *Ferroelectrics* **2011**, *336*, 137–144. [CrossRef]

51. Narvaez, J.; Catalan, G. Origin of the enhanced flexoelectricity of relaxor ferroelectrics. *Appl. Phys. Lett.* **2014**, *104*, 162903. [CrossRef]

52. Shu, L.; Wan, M.; Jiang, X.; Li, F.; Zhou, N.; Huang, W.; Wang, T. Frequency dispersion of flexoelectricity in PMN-PT single crystal. *AIP Adv.* **2017**, *7*, 015010. [CrossRef]

53. Shu, L.; Li, T.; Wang, Z.; Li, F.; Fei, L.; Rao, Z.; Ye, M.; Ke, S.; Huang, W.; Wang, Y.; et al. Flexoelectric behavior in PIN-PMN-PT single crystals over a wide temperature range. *Appl. Phys. Lett.* **2017**, *111*, 162901. [CrossRef]

54. Li, C.; Wang, Z.; Li, F.; Rao, Z.; Huang, W.; Shen, Z.; Ke, S.; Shu, L. Large flexoelectric response in PMN-PT ceramics through composition design. *Appl. Phys. Lett.* **2019**, *115*, 142901. [CrossRef]

55. Yu, Z.; Wang, Z.; Shu, S.; Tian, T.; Huang, W.; Li, C.; Ke, S.; Shu, L. Local structural heterogeneity induced large flexoelectricity in Sm-doped PMN–PT ceramics. *J. Appl. Phys.* **2021**, *129*, 174103. [CrossRef]

56. Ma, W.; Cross, L.E. Flexoelectric effect in ceramic lead zirconate titanate. *Appl. Phys. Lett.* **2005**, *86*, 072905. [CrossRef]

57. Henmi, N.; Tohyama, M. Measurement of Flexoelectric Effect in Lead Zirconate Titanate Ceramics. *J. Adv. Mech. Design Syst. Manuf.* **2011**, *5*, 1–6. [CrossRef]

58. Vales-Castro, P.; Roleder, K.; Zhao, L.; Li, J.-F.; Kajewski, D.; Catalan, G. Flexoelectricity in antiferroelectrics. *Appl. Phys. Lett.* **2018**, *113*, 132903. [CrossRef]

59. Zhou, W.; Hou, Y.; Chen, P.; Zhang, H.; Chu, B. The surface mechanism for the flexoelectric response in sodium bismuth titanate-based ferroelectric ceramics. *J. Am. Ceram. Soc.* **2019**, *102*, 5454–5464. [CrossRef]

60. Zhang, H.; Chu, B. Energy harvesting by exploiting the enhanced flexoelectric-like response of reduced $(Na_{0.5}Bi_{0.5})_{0.92}Ba_{0.08}TiO_3$ ceramics. *J. Eur. Ceram. Soc.* **2018**, *38*, 2520–2525. [CrossRef]

61. Zhou, W.; Chen, P.; Pan, Q.; Zhang, X.; Chu, B. Lead-Free Metamaterials with Enormous Apparent Piezoelectric Response. *Adv. Mater.* **2015**, *27*, 6349–6355. [CrossRef] [PubMed]

62. Pan, Q.; Fang, C.; Luo, H.; Chu, B. Magnetoelectric response from the enhanced ferromagnetism and flexoelectric response in reduced BiFeO$_3$–based ceramics. *J. Eur. Ceram. Soc.* **2019**, *39*, 1057–1064. [CrossRef]
63. Li, Y.; Shu, L.; Zhou, Y.; Guo, J.; Xiang, F.; He, L.; Wang, H. Enhanced flexoelectric effect in a non-ferroelectric composite. *Appl. Phys. Lett.* **2013**, *103*, 142909. [CrossRef]
64. Zhu, J.; Chen, T.; Shu, L.; Wang, Z.; Huang, W.; Fei, L.; Li, F.; Rao, Z.; Ke, S.; Li, B.; et al. Flexoelectric fatigue in (K,Na,Li)(Nb,Sb)O$_3$ ceramics. *Appl. Phys. Lett.* **2018**, *113*, 182901. [CrossRef]
65. Poddar, S.; Ducharme, S. Measurement of the flexoelectric response in ferroelectric and relaxor polymer thin films. *Appl. Phys. Lett.* **2013**, *103*, 202901. [CrossRef]
66. Zhang, S.; Xu, M.; Ma, G.; Liang, X.; Shen, S. Experimental method research on transverse flexoelectric response of poly(vinylidene fluoride). *Jpn. J. Appl. Phys.* **2016**, *55*, 071601. [CrossRef]
67. Zhou, Y.; Liu, J.; Hu, X.; Chu, B.; Chen, S.; Salem, D. Flexoelectric effect in PVDF-based polymers. *IEEE Trans. Dielectr. Electr. Insul.* **2017**, *24*, 727–731. [CrossRef]
68. Hu, X.; Zhou, Y.; Liu, J.; Chu, B. Improved flexoelectricity in PVDF/barium strontium titanate (BST) nanocomposites. *J. Appl. Phys.* **2018**, *123*, 154101. [CrossRef]
69. Liu, J.; Zhou, Y.; Hu, X.; Chu, B. Flexoelectric effect in PVDF-based copolymers and terpolymers. *Appl. Phys. Lett.* **2018**, *112*, 232901. [CrossRef]
70. Wen, X.; Yang, G.; Ma, Q.; Tian, Y.; Liu, X.; Xue, D.; Deng, Q.; Shen, S. Flexoelectricity in compositionally graded Ba$_{1-x}$SrxTiO$_3$ ceramics. *J. Appl. Phys.* **2021**, *130*, 074102. [CrossRef]
71. Tagantsev, A.K. Piezoelectricity and flexoelectricity in crystalline dielectrics. *Phys. Rev. B* **1987**, *36*, 6177. [CrossRef] [PubMed]
72. Tagantsev, A.K.; Yurkov, A.S. Flexoelectric effect in finite samples. *J. Appl. Phys.* **2012**, *112*, 044103. [CrossRef]
73. Stengel, M. Microscopic response to inhomogeneous deformations in curvilinear coordinates. *Nat. Commun.* **2013**, *4*, 2693. [CrossRef] [PubMed]
74. Stengel, M. Surface control of flexoelectricity. *Phys. Rev. B* **2014**, *90*, 201112. [CrossRef]
75. Hong, J.; Vanderbilt, D. First-principles theory of frozen-ion flexoelectricity. *Phys. Rev. B* **2011**, *84*, 180101. [CrossRef]
76. Tian, D.; Chen, P.; Yang, X.; Chu, B. Thickness dependence of dielectric and piezoelectric properties from the surface layer effect of BaTiO$_3$-based ceramics. *Ceram. Int.* **2021**, *47*, 17262–17267. [CrossRef]
77. Narvaez, J.; Vasquez-Sancho, F.; Catalan, G. Enhanced flexoelectric-like response in oxide semiconductors. *Nature* **2016**, *538*, 219–221. [CrossRef]
78. Shu, L.; Ke, S.; Fei, L.; Huang, W.; Wang, Z.; Gong, J.; Jiang, X.; Wang, L.; Li, F.; Lei, S.; et al. Photoflexoelectric effect in halide perovskites. *Nat. Mater.* **2020**, *19*, 605–609. [CrossRef]
79. Garten, L.M.; Trolier-McKinstry, S. Enhanced flexoelectricity through residual ferroelectricity in barium strontium titanate. *J. Appl. Phys.* **2015**, *117*, 094102. [CrossRef]
80. Liu, X.; Tan, P.; Ma, X.; Wang, D.; Jin, X.; Liu, Y.; Xu, B.; Qiao, L.; Qiu, C.; Wang, B.; et al. Ferroelectric crystals with giant electro-optic property enabling ultracompact Q-switches. *Science* **2022**, *376*, 371–377. [CrossRef]
81. Wu, M.; Zhang, X.; Li, X.; Qu, K.; Sun, Y.; Han, B.; Zhu, R.; Gao, X.; Zhang, J.; Liu, K.; et al. Engineering of atomic-scale flexoelectricity at grain boundaries. *Nat. Commun.* **2022**, *13*, 216. [CrossRef] [PubMed]
82. Lee, D.; Yoon, A.; Jang, S.Y.; Yoon, J.G.; Chung, J.S.; Kim, M.; Scott, J.F.; Noh, T.W. Giant flexoelectric effect in ferroelectric epitaxial thin films. *Phys. Rev. Lett.* **2011**, *107*, 057602. [CrossRef]
83. Wang, Z.; Li, C.; Zhang, Z.; Hu, Y.; Huang, W.; Ke, S.; Zheng, R.-K.; Li, F.; Shu, L. Interplay of defect dipole and flexoelectricity in linear dielectrics. *Scr. Mater.* **2022**, *210*, 114427. [CrossRef]
84. Li, Q.; Liu, Y.; Liu, J.; Song, K.; Guo, H.; Li, F.; Xu, Z. Enhanced Piezoelectric Properties and Improved Property Uniformity in Nd-Doped PMN-PT Relaxor Ferroelectric Single Crystals. *Adv. Funct. Mater.* **2022**, *32*, 202201719. [CrossRef]
85. Das, S.; Wang, B.; Paudel, T.R.; Park, S.M.; Tsymbal, E.Y.; Chen, L.Q.; Lee, D.; Noh, T.W. Enhanced flexoelectricity at reduced dimensions revealed by mechanically tunable quantum tunnelling. *Nat. Commun.* **2019**, *10*, 537. [CrossRef]
86. Yamada, T.; Astafiev, K.F.; Sherman, V.O.; Tagantsev, A.K.; Muralt, P.; Setter, N. Strain relaxation of epitaxial SrTiO$_3$ thin films on LaAlO$_3$ by two-step growth technique. *Appl. Phys. Lett.* **2005**, *86*, 142904. [CrossRef]
87. Catalan, G.; Noheda, B.; McAneney, J.; Sinnamon, L.J.; Gregg, J.M. Strain gradients in epitaxial ferroelectrics. *Phys. Rev. B* **2005**, *72*, 020102. [CrossRef]
88. Karthik, J.; Mangalam, R.V.K.; Agar, J.C.; Martin, L.W. Large built-in electric fields due to flexoelectricity in compositionally graded ferroelectric thin films. *Phys. Rev. B* **2013**, *87*, 024111. [CrossRef]
89. Park, S.M.; Wang, B.; Paudel, T.; Park, S.Y.; Das, S.; Kim, J.R.; Ko, E.K.; Lee, H.G.; Park, N.; Tao, L.; et al. Colossal flexoresistance in dielectrics. *Nat. Commun.* **2020**, *11*, 2586. [CrossRef]
90. Sun, L.; Zhu, L.; Zhang, C.; Chen, W.; Wang, Z. Mechanical Manipulation of Silicon-based Schottky Diodes via Flexoelectricity. *Nano Energy* **2021**, *83*, 105855. [CrossRef]
91. Guo, R.; You, L.; Lin, W.; Abdelsamie, A.; Shu, X.; Zhou, G.; Chen, S.; Liu, L.; Yan, X.; Wang, J.; et al. Continuously controllable photoconductance in freestanding BiFeO$_3$ by the macroscopic flexoelectric effect. *Nat. Commun.* **2020**, *11*, 2571. [CrossRef] [PubMed]
92. Park, S.M.; Wang, B.; Chen, L.-Q.; Noh, T.W.; Yang, S.M.; Lee, D. Flexoelectric control of physical properties by atomic force microscopy. *Appl. Phys. Rev.* **2021**, *8*, 041327. [CrossRef]

93. Lee, D.; Yang, S.M.; Yoon, J.G.; Noh, T.W. Flexoelectric rectification of charge transport in strain-graded dielectrics. *Nano Lett.* **2012**, *12*, 6436–6440. [CrossRef] [PubMed]

94. Zhang, F.; Lv, P.; Zhang, Y.; Huang, S.; Wong, C.M.; Yau, H.M.; Chen, X.; Wen, Z.; Jiang, X.; Zeng, C.; et al. Modulating the Electrical Transport in the Two-Dimensional Electron Gas at $LaAlO_3/SrTiO_3$ Heterostructures by Interfacial Flexoelectricity. *Phys. Rev. Lett.* **2019**, *122*, 257601. [CrossRef] [PubMed]

95. Majdoub, M.S.; Sharma, P.; Cagin, T. Enhanced size-dependent piezoelectricity and elasticity in nanostructures due to the flexoelectric effect. *Phys. Rev. B* **2009**, *79*, 119904. [CrossRef]

96. Liu, C.; Wu, H.; Wang, J. Giant piezoelectric response in piezoelectric/dielectric superlattices due to flexoelectric effect. *Appl. Phys. Lett.* **2016**, *109*, 192901. [CrossRef]

97. Catalan, G.; Lubk, A.; Vlooswijk, A.H.; Snoeck, E.; Magen, C.; Janssens, A.; Rispens, G.; Rijnders, G.; Blank, D.H.; Noheda, B. Flexoelectric rotation of polarization in ferroelectric thin films. *Nat. Mater.* **2011**, *10*, 963–967. [CrossRef]

98. Gruverman, A.; Rodriguez, B.J.; Kingon, A.I.; Nemanich, R.J.; Tagantsev, A.K.; Cross, J.S.; Tsukada, M. Mechanical stress effect on imprint behavior of integrated ferroelectric capacitors. *Appl. Phys. Lett.* **2003**, *83*, 728–730. [CrossRef]

99. Liu, J.-H.; Chen, X.; Li, Y.; Guo, X.; Ge, H.-X.; Shen, Q.-D. Ferroelectric polymer nanostructure with enhanced flexoelectric response for force-induced memory. *Appl. Phys. Lett.* **2018**, *113*, 042903. [CrossRef]

100. Lee, D.; Jeon, B.C.; Yoon, A.; Shin, Y.C.; Lee, M.H.; Song, T.K.; Bu, S.D.; Kim, M.; Chung, J.-S.; Yoon, J.G.; et al. Flexoelectric Control of Defect Formation in Ferroelectric Epitaxial Thin Films. *Adv. Mater.* **2014**, *26*, 5005–5011. [CrossRef]

101. Das, S.; Wang, B.; Cao, Y.; Rae Cho, M.; Jae Shin, Y.; Mo Yang, S.; Wang, L.; Kim, M.; Kalinin, S.V.; Chen, L.Q.; et al. Controlled manipulation of oxygen vacancies using nanoscale flexoelectricity. *Nat. Commun.* **2017**, *8*, 615. [CrossRef] [PubMed]

102. Jia, T.; Kimura, H.; Cheng, Z.; Zhao, H.; Kim, Y.-H.; Osada, M.; Matsumoto, T.; Shibata, N.; Ikuhara, Y. Mechanical force involved multiple fields switching of both local ferroelectric and magnetic domain in a $Bi_5Ti_3FeO_{15}$ thin film. *NPG Asia Mater.* **2017**, *9*, e349. [CrossRef]

103. Gharbi, M.; Sun, Z.H.; Sharma, P.; White, K.; El-Borgi, S. Flexoelectric properties of ferroelectrics and the nanoindentation size-effect. *Int. J. Solids Struct.* **2011**, *48*, 249–256. [CrossRef]

104. Hu, T.; Deng, Q.; Shen, S. Probing flexoelectricity via a split Hopkinson pressure bar experiment. *Appl. Phys. Lett.* **2018**, *112*, 242902. [CrossRef]

105. Wu, M.; Jiang, Z.; Lou, X.; Zhang, F.; Song, D.; Ning, S.; Guo, M.; Pennycook, S.J.; Dai, J.Y.; Wen, Z. Flexoelectric Thin-Film Photodetectors. *Nano Lett.* **2021**, *21*, 2946–2952. [CrossRef] [PubMed]

106. Chen, P.; Zhang, H.; Chu, B. Strain gradient induced thermal-electrical response in paraelectric $Na_{0.5}Bi_{0.5}TiO_3$-based ceramics. *Phys. Rev. Mater.* **2018**, *2*, 034401. [CrossRef]

107. Chen, P.; Zhou, W.; Zhang, H.; Pan, Q.; Zhang, X.; Chu, B. Large Thermal–Electrical Response and Rectifying Conduction Behavior in Asymmetrically Reduced Ferroelectric Ceramics. *ACS Appl. Electron. Mater.* **2019**, *1*, 478–484. [CrossRef]

108. Qi, M.; Yang, Z.; Chen, S.; Lin, S.; Jin, Q.; Hong, H.; Rong, D.; Guo, H.; Wang, C.; Wang, Z.; et al. Asymmetric ground states in $La_{0.67}Sr_{0.33}MnO_3/BaTiO_3$ heterostructures induced by flexoelectric bending. *Appl. Phys. Lett.* **2022**, *120*, 233103. [CrossRef]

109. Mizzi, C.A.; Lin, A.Y.W.; Marks, L.D. Does Flexoelectricity Drive Triboelectricity? *Phys. Rev. Lett.* **2019**, *123*, 116103. [CrossRef]

110. Persson, B.N.J. On the role of flexoelectricity in triboelectricity for randomly rough surfaces. *EPL* **2020**, *129*, 10006. [CrossRef]

111. Zhu, W.; Fu, J.Y.; Li, N.; Cross, L. Piezoelectric composite based on the enhanced flexoelectric effects. *Appl. Phys. Lett.* **2006**, *89*, 192904. [CrossRef]

112. Tian, D.; Hou, Y.; Pan, Q.; Chu, B. Large Piezoelectriclike Response from Inhomogeneously Deformed Silicon Crystals. *Phys. Rev. Appl.* **2020**, *14*, 034008. [CrossRef]

113. Jiang, X.; Huang, W.; Zhang, S. Flexoelectric nano-generator: Materials, structures and devices. *Nano Energy* **2013**, *2*, 1079–1092. [CrossRef]

114. Huang, W.; Yan, X.; Kwon, S.R.; Zhang, S.; Yuan, F.-G.; Jiang, X. Flexoelectric strain gradient detection using $Ba_{0.64}Sr_{0.36}TiO_3$ for sensing. *Appl. Phys. Lett.* **2012**, *101*, 252903. [CrossRef]

115. Huang, W.; Kwon, S.-R.; Zhang, S.; Yuan, F.-G.; Jiang, X. A trapezoidal flexoelectric accelerometer. *J. Intell. Mater. Syst. Struct.* **2013**, *25*, 271–277. [CrossRef]

116. Kwon, S.R.; Huang, W.B.; Zhang, S.J.; Yuan, F.G.; Jiang, X.N. Study on a flexoelectric microphone using barium strontium titanate. *J. Micromech. Microeng.* **2016**, *26*, 045001. [CrossRef]

117. Zhou, W.; Chu, B. Sodium bismuth titanate-based lead-free RAINBOW piezoelectric devices. *J. Eur. Ceram. Soc.* **2017**, *37*, 2373–2377. [CrossRef]

118. Zhang, S.; Zhai, C.; Liu, K.; Song, S.; Ji, H.; Shao, S.; Xu, M. Quantitative evaluation of energy harvesting capabilities on flexoelectric and piezoelectric materials. *J. Appl. Phys.* **2022**, *131*, 064101. [CrossRef]

119. Qi, Y.; Jafferis, N.T.; Lyons, K., Jr.; Lee, C.M.; Ahmad, H.; McAlpine, M.C. Piezoelectric ribbons printed onto rubber for flexible energy conversion. *Nano Lett.* **2010**, *10*, 524–528. [CrossRef]

120. Xu, R.; Chen, P.; Chen, C.; Hou, Y.; Chu, B. Thermal-electrical like response in doped sodium bismuth titanate-based ferroelectric ceramics. *Ceram. Int.* **2022**, *48*, 27568–27574. [CrossRef]

121. Jiang, J.; Chen, Z.; Hu, Y.; Xiang, Y.; Zhang, L.; Wang, Y.; Wang, G.C.; Shi, J. Flexo-photovoltaic effect in MoS_2. *Nat. Nanotechnol.* **2021**, *16*, 894–901. [CrossRef]

122. Jiang, Z.; Xu, Z.; Xi, Z.; Yang, Y.; Wu, M.; Li, Y.; Li, X.; Wang, Q.; Li, C.; Wu, D.; et al. Flexoelectric-induced photovoltaic effects and tunable photocurrents in flexible LaFeO$_3$ epitaxial heterostructures. *J. Mater.* **2022**, *8*, 281–287. [CrossRef]

123. Jin, Y.; Zhang, F.; Zhou, K.; Suen, C.H.; Zhou, X.Y.; Dai, J.-Y. Oxygen vacancy and photoelectron enhanced flexoelectricity in perovskite SrTiO$_3$ crystal. *Appl. Phys. Lett.* **2021**, *118*, 164101. [CrossRef]

124. Qiao, H.; Zhao, P.; Kwon, O.; Sohn, A.; Zhuo, F.; Lee, D.-M.; Sun, C.; Seol, D.; Lee, D.; Kim, S.-W.; et al. Mixed triboelectric and flexoelectric charge transfer at the nanoscal. *Adv. Sci.* **2021**, *8*, 2101793. [CrossRef] [PubMed]

125. Liu, L.; Chen, W.; Zheng, Y. Flexoresponses of Synthetic Antiferromagnetic Systems Hosting Skyrmions. *Phys. Rev. Lett.* **2022**, *128*, 257201. [CrossRef] [PubMed]